AGU PUBLICATIONS

Geochemistry, Geophysics, Geosystems

RESEARCH ARTICLE
10.1002/2016GC006444

Effect of melt composition on crustal carbonate assimilation: Implications for the transition from calcite consumption to skarnification and associated CO_2 degassing

Laura B. Carter[1] and Rajdeep Dasgupta[1]

[1]Department of Earth Science, Rice University, Houston, Texas, USA

Key Points:
- Limestone assimilation increases with infiltration of hydrous andesitic melt over basaltic but decreases with dacite
- Skarn minerals like wollastonite increase in abundance in more silicic magma-calcite interaction
- Assimilation can release <~0.4 Gt CO_2 during intruding magma evolution from basalt to granite

Supporting Information:
- Supporting Information S1
- Table S1

Correspondence to:
L. B. Carter,
Laura.B.Carter@rice.edu

Citation:
Carter, L. B., and R. Dasgupta (2016), Effect of melt composition on crustal carbonate assimilation: Implications for the transition from calcite consumption to skarnification and associated CO_2 degassing, *Geochem. Geophys. Geosyst.*, *17*, 3893–3916, doi:10.1002/2016GC006444.

Received 18 MAY 2016
Accepted 9 SEP 2016
Accepted article online 20 SEP 2016
Published online 13 OCT 2016

Abstract Skarns are residue of relatively low-temperature magma-induced decarbonation in the crust largely associated with silicic plutons. Mafic magmatic intrusions are also capable of releasing excess CO_2 due to carbonate assimilation. However, the effect of mafic to silicic melt evolution on the decarbonation processes, in addition to temperature controls on carbonate-intrusive magmatic systems, particularly at continental arcs, remains unclear. In this study, experiments performed in a piston cylinder apparatus at mid-crustal depth (0.5 GPa) at supersolidus temperatures (900–1200°C) document calcite interaction with andesite and dacite melts at equilibrium under closed-system conditions at calcite saturation in a 1:1 melt-calcite ratio by weight. With increasing silica content in the starting melt, at similar melt fractions and identical pressure, assimilation decreases drastically ($\leq$65% andesite-calcite to $\leq$18% dacite-calcite). In conjunction, the CaO/SiO_2 ratio in melts resulting from calcite assimilation in andesitic starting material is >1, but $\leq$0.3 in those formed from dacite-calcite interaction. With increasing silica-content in the starting melt skarn mineralogy, particularly wollastonite, increases in modal abundance while diopsidic clinopyroxene decreases slightly. More CO_2 is released with andesite-calcite reaction ($\leq 2.9 \times 10^{11}$ g/y) than with more skarn-like dacite-calcite interaction ($\leq 8.1 \times 10^{10}$ g/y, at one volcano assuming respective calcite-free-superliquidus conditions and a magma flux of 10^{12} g/y). Our experimental results thus suggest that calcite assimilation in more mafic magmas may have first degassed a significant amount of crustal carbon before the melt evolves to more silicic compositions, producing skarn. Crustal decarbonation in long-lived magmatic systems may hence deliver significant albeit diminishing amounts of carbon to the atmosphere and contribute to long-term climate change.

1. Introduction

Intrusion of subduction zone magma into crustal carbonates can induce magma-wall rock interaction in one of two ways: (1) consumption of carbonate by assimilation, producing silica-undersaturated, ultracalcic melts, and carbon dioxide vapor that can easily degas at the volcanic edifice; and/or (2) metasomatic skarnification producing calc-silicate mineralogy and releasing carbon dioxide that can be transported as a fluid to the surface via fractures in the crust. The first has been identified and experimentally studied with regard to carbon dioxide degassing of a few presently active volcanic systems with high-temperature mafic magmas. The second, associated with granitic plutons, has been petrologically well documented in the field, particularly by economic geologists with regard to ore deposits, but poorly constrained in terms of past contribution to atmospheric CO_2. It remains unclear if and how the two processes are linked and whether the evolution of the magma as it ascends through the crust affects the likelihood of one process over the other.

For many years economic geologists have studied carbonate-magma interaction with little attention to the skarn mineralogy and composition beyond the seven elements of economic importance: Au, W, Zn, Mo, Cu, Sn, and Fe [*Meinert et al.*, 2005]. In recent years, carbonate assimilation has been the focus of geochemical and experimental investigation in currently active volcanic systems, including Etna [*Chiodini et al.*, 2010; *Mollo et al.*, 2010b]; Merapi [*Chadwick et al.*, 2007; *Deegan et al.*, 2010; *Troll et al.*, 2012, 2013; *Nadeau et al.*, 2013a; *Blythe et al.*, 2015]; Vesuvius [*Barberi and Leoni*, 1980; *Fulignati et al.*, 2000, 2005; *Del Moro et al.*, 2001; *Gilg et al.*, 2001; *Piochi et al.*, 2006; *Iacono-Marziano et al.*, 2009; *Dallai et al.*, 2011; *Jolis et al.*, 2013, 2015]; Popocatepetl [*Goff et al.*, 1998, 2001; *Schaaf et al.*, 2005]; the Colli Albani Volcanic District (CAVD) [e.g., *Gaeta et al.*, 2000; *Chiodini and Frondini*, 2001; *Freda et al.*, 2008; *Di Rocco et al.*, 2012], or more general primitive

magma-limestone interaction [*Carter and Dasgupta*, 2015]. In addition to consumption, both heat and aqueous fluids can be released from an intruding magma and react with the country rock in a wide aureole [e.g., *Bergantz*, 2000], decarbonating the wall-rock and leaving residual calc-silicate skarns behind [*Kerrick*, 1977; *Einaudi et al*., 1981; *Fulignati et al*., 2000, 2005; *Gilg et al*., 2001; *Jolis et al*., 2015]. This breakdown can be identified through diffuse CO_2 degassing as seen at the surface today, for example, in Italy or the East African Rift Zone [*Chiodini et al*., 1995, 2004, 2010; *Chiodini and Frondini*, 2001; *Frondini et al*., 2004; *Caliro et al*., 2005, 2014; *Toutain et al*., 2009; *Parks et al*., 2013; *Granieri et al*., 2013; *Afanasyev et al*., 2015; *Lee et al*., 2016] but may also have been significant through time [*Kerrick and Caldeira*, 1998; *Kerrick*, 2001; *Lackey et al*., 2005; *Evans et al*., 2008; *Ganino and Arndt*, 2009; *Johnston et al*., 2011; *Groppo et al*., 2013; *Lee et al*., 2013; *Lee and Lackey*, 2015].

Despite progress made, lingering questions regarding magma-carbonate interaction include: under what conditions does assimilation prevail over skarnification, and is there a bridge between the two? Some combination of duration of interaction, degassing efficiency, open versus closed-system conditions, mineralogy, and/or pressure-temperature-compositional conditions likely govern the transition from magmatic consumption to metasomatic and metamorphic decarbonation. For the most part skarns are associated with neighboring silicic (granitic) plutons [*Kerrick*, 1977; *Moine*, 1979; *Einaudi et al*., 1981; *Einaudi and Burt*, 1982a; *Meinert*, 1992; *Meinert et al*., 2005], which suggests that perhaps more evolved magmas, or simply those that reside in a magma body in the crust long enough to evolve to silicic compositions have enough time to interact with the wall-rock. On the other hand, assimilation is thought to be an extremely rapid process with basaltic magma [*Deegan et al*., 2010, 2011; *Sottili et al*., 2010; *Jolis et al*., 2013], which may suggest the opposite could also be true. The evolved magma is likely cooler, shallower, and more viscous, and thereby may inhibit direct assimilation but facilitate metasomatic infiltration of fluids.

By controlling and changing intensive variables, experimental work can constrain the dominant effects on the transition from assimilation to skarnification. Focusing on present-day natural systems, most previous experimental studies simulated the low pressure ($\leq$0.5 GPa), high temperature (1050–1400°C), and narrow melt compositional (basalt, trachybasalt, phonotephrite) conditions of Italian [*Iacono-Marziano et al*., 2007, 2008; *Freda et al*., 2008; *Conte et al*., 2009; *Mollo et al*., 2010a; *Jolis et al*., 2013] and Indonesian [*Deegan et al*., 2010] magma-crust systems, with variable water contents (0–6 wt.%) and limited carbonate addition ($<$20 wt.%). A recent study systematically investigated varying pressure and temperature (0.5–1.0 GPa, 1100–1200°C) on calcite assimilation with a typical hydrous arc basaltic composition and concluded that up to 47.6% assimilation was possible [*Carter and Dasgupta*, 2015].

In this study, we investigate the effect of melt composition on calcite assimilation from supraliquidus to near-solidus temperatures, based on each composition's respective liquid line of descent at low pressure ($\sim$15 km). Carbonate composition was constant (pure calcite), and layered in equal proportion (by weight) with a silicate starting material to simulate the intrusion-wall rock interface. We compare our results generated using intermediate (andesite) and silicic (dacite) starting compositions to those generated by mafic (basalt)-calcite interaction [*Carter and Dasgupta*, 2015] as well as natural skarns. We also consider CO_2 release in order to estimate calcite consumption at active volcanic arcs with various melt compositions and determine a simple estimate of total decarbonation within the ascending, cooling, evolving, and crystallizing lifespan of past plutonic intrusions. This experimental study suggests that melt composition and melt fraction may be controlling factors in the transition from assimilation to skarnification in magma-calcite interaction.

2 Methods

2.1. Starting Materials

Two different magmatic compositions were used (Table 1). The first, a synthetic hydrous andesite, closely resembles the average from the primitive arc andesite global compilation of *Kelemen et al*. [2014]. The second composition is a hydrous dacite and loosely resembles natural dacites found in the Cascades, the Andes, and arcs in Japan and Indonesia [*Miyashiro*, 1974; *Hammer et al*., 2000; *Ohlhorst et al*., 2001; *Grove et al*., 2005; *Prouteau et al*., 1999].

Before being weighed in a microbalance and mixed under ethanol in an agate mortar, reagent grade oxides and carbonates were fired overnight: SiO_2, TiO_2, Al_2O_3, and MgO at 1000°C, Fe_2O_3 at 800°C, MnO_2 at 400°C,

Table 1. Starting Melt Compositions[a]

Reference Source	This Study	Kelemen14 Arc Average	Ohlhorst01 Mt Unzen, Japan	This Study	Miyashiro74 Arc Average	Grove05 Mt Shasta, USA	Prouteau99 Mt Pinatubo, Philippines
(wt.%)	Andesite	Andesite	Andesite	Dacite	Dacite	Dacite	Dacite
SiO_2	59.68	58.05	57.21	67.02	68.16	64.31	64.60
TiO_2	0.79	0.79	0.84	0.69	0.43	0.51	0.53
Al_2O_3	14.09	15.96	17.50	14.53	15.19	16.60	16.50
FeO_T[b]	6.31	6.14	7.58	4.37	3.19	4.52	4.37
MnO	0.14	0.12	0.11	0.07	0.09	0.07	
MgO	6.50	6.56	4.27	1.87	1.16	2.82	2.39
CaO	7.56	7.20	7.59	4.95	3.40	5.25	5.23
Na_2O	3.31	3.31	3.31	4.00	3.21	4.37	4.49
K_2O	1.39	1.67	1.60	2.29	1.77	1.41	1.54
P_2O_5	0.24	0.22		0.21	0.15	0.15	
Sum[c]	100.00	100.02	100.01	100	99.84	99.31	99.31
H_2O[d]	5.86			2.97			

[a]All values for major elements given in volatile-free wt.% as determined in This Study by weighed proportions of synthetic powders (see Methods) and as reported in the literature for previous studies (Miyashiro74 = *Miyashiro* [1974]; Ohlhorst01 = *Ohlhorst et al.* [2001]; Grove05 = *Grove et al.* [2005]; Prouteau99= *Prouteau et al.* [1999]; Kelemen14 = *Kelemen et al.* [2014]). The bulk silicate composition of starting materials based on weighing are in good agreement with the silicate glass compositions measured using EPMA (Table 2).

[b]FeO_T refers to total iron.

[c]Indicates volatile-free sum of given major elements.

[d]Amount of water added to the hydrous starting melts.

$CaCO_3$ at 250°C, and K_2CO_3 and Na_2CO_3 at 110°C to drive off adsorbed water. The homogenized powder mix was then decarbonated and reduced to convert Fe_2O_3 to FeO at 1000°C and log fO_2 ~FMQ-2 in a CO-CO_2 gas mixing vertical tube furnace for 24 h. As a last step, the powders were reground with gibbsite [$Al(OH)_3$], which provided ~3–5 wt.% water to each of the hydrous melts (Table 1). Due to the proximity of the dacite liquidus to the temperature of decarbonation and reduction in the gas mixing furnace, a platinum crucible was used which absorbed some of the iron from the powder. Therefore, an additional ~1.5 wt.% iron, as Fe_2O_3, was added to the dacite powder. To mimic the limestone wall-rock, reagent grade $CaCO_3$ powder was used in layered experiments. To limit water adsorption, all starting materials were covered and stored in a 110°C oven.

2.2. Experimental Methods

Following the methods performed for basalt-calcite interaction experiments documented in *Carter and Dasgupta* [2015], two sets of experiments were performed for each silicate starting material using a $^1/_2$-inch bore pressure vessel in a piston cylinder apparatus at Rice University. In the first, to discern the liquid line of descent, silicate starting materials were run alone. In the second, calcite powder was overlain by an equal proportion by weight (within 0.1 wt.% error) of powdered silicate starting material to simulate a magma-wall rock interface. Most experiments were packed in 3 mm-outer diameter $Au_{75}Pd_{25}$ capsules; however, several were instead packed in 2 mm-outer diameter capsules and run in pairs, side-by-side to ensure identical *P-T* conditions. The capsules were nestled in crushable MgO surrounded by graphite and $BaCO_3$ sleeves with an outer Pb-foil to decrease the effect of friction. The pressure and temperature calibration and uncertainty (pressure had $\leq$4% error during runs, while temperature was within $\pm$10°C of the set target) of this assemblage is detailed in *Tsuno and Dasgupta* [2011] and detailed run procedures are reported in several recent studies [e.g., *Mallik and Dasgupta*, 2014; *Carter and Dasgupta*, 2015; *Duncan and Dasgupta*, 2015]. Experimental run conditions are given in Table 2. This study considered a pressure-range relevant for mid-crustal intrusions of 0.5 GPa (~15 km deep), with a few additional experiments at 0.8 GPa, and 1.0 GPa (~35 km deep) to determine pressure effects. Temperature conditions were between 900 and 1200°C. Experiments reached target pressure-temperature conditions using the cold-piston-in method with a steady heating rate of 100°C/min. Temperature was monitored and maintained with a Type-C thermocouple. For the first few hours, pressure was controlled manually and later by automated control that kept the experiment within $\sim 6 \times 10^{-5}$ GPa. After 24–120 h depending on temperature, experiments were terminated by switching off power to the heating element that resulted in cooling of the charges to $<$100°C in $<$10 s. For analysis, extracted capsules were mounted in epoxy and ground in half to expose the run products using dry silicon-carbide sandpaper. Run products were impregnated with epoxy and reground, with a final dry polycrystalline diamond powder (3, 1, 0.25 μm) polish on nylon and velvet surfaces.

AGU Geochemistry, Geophysics, Geosystems 10.1002/2016GC006444

Table 2. Experimental Run Conditions, Obtained Phase Assemblages, and Average Proportions of Phases (wt.%)

Experiment No.	*P* (GPa)	*T* (°C)	Duration (h)	[a]Opx	Qz	Il	Sp	Plag	Sc	Cpx	Wo	Melt	Cc	[b]ΣR^2
Experiments with Andesite Starting Material														
B343	0.5	1075	56	10.4	0.0		3.1	26.3		28.7		31.4		0.2 (3)
B328	0.5	1100	48	6.6			2.7[c]	16.7 (2)		20.2		53.8(2)		0.1 (7)
B334	0.5	1125	24	5.5			3.0[c]	21.2		8.6		61.6		0.9 (5)
B335	0.5	1150	24	5.5			1.6[c]	0.4		9.8		82.7		0.2 (2)
B347	0.5	1175	24	8.2				3.6		4.0		84.2		0.1 (2)
B310	0.5	1200	3									100		0 (2)
B369[d]	0.5	1050	96		5.2			19.8		13.2		11.0	50.8	0.1 (4)
B348[d]	0.5	1075	24		0.0		3.1[c]	4.7		15.9	0.1	26.6	49.6	0.3 (3)
B341A[d]	0.5	1075	48		0.3		3.9	4.6		16.8		24.5	49.9	0.1
B340[d]	0.5	1075	96				2.9	3.5		15.2		28.5	49.9	0.8 (1)
B324[b]	0.5	1100	48				3.7[c]	3.9	0.1	9.7	0.1	33.2	49.3	1.9 (2)
B326[d]	0.5	1125	24					0.0	0.6	4.1	0.0[c]	61.6	33.7	1.3 (10)
B325[d]	0.5	1150	24					0.0	0.0	0.8	1.8	75.1	22.3	0.5 (3)
B344B[d]	0.5	1175	24								0.0[c]	82.2	17.8	0.1 (5)
B317[d]	0.5	1200	24								3.9[c]	75.4	20.7	1.1 (6)
B313[d]	0.8	1200	24									79.1	20.9	0.1 (4)
B318[d]	1	1200	24							2.8		72.8	24.4	0.7 (4)
Experiments with Dacite Starting Material														
B382A	0.5	900	72		8.2[a]		1.9[a]	38.8		13		38.1		0.8 (6)
B377	0.5	1000	72		+	+	+	+		+		+		
B380A	0.5	1100	24									100.0		1.8 (3)
B392[d]	0.5	900	120		12.3	0.5	4.3[c]	1.0		5	0.9	25.6	50.4	0.7 (2)
B381[d]	0.5	1000	72		0.9		6.5[c]	1.0		4.0	17.9	26.8	42.9	1.2
B380B[d]	0.5	1100	24		0.0		5.0	1.0		2.9	19.4	30.7	41.0	1.9

[a]Resulting run phases all in wt.%, where 0.0 indicates presence in trace amounts, with $\pm 1\sigma$ error (calculated by Monte Carlo simulations using compositional standard deviation of replicate volatile-free analysis of each phase within a run) reported where nonnegligible in parentheses to the last digit provided; e.g., 0.2(3) is 0.2 $\pm$0.3 wt.%. Phases include: Opx = orthopyroxene, Qz = quartz, Il = Ilmenite, Sp = spinel, Plag = Plagioclase, Sc = scapolite, Cpx = clinopyroxene, Wo = wollastonite, Melt, and Cc = calcite.

[b]Calculated ΣR^2 value is the sum of squared residuals from mass balance calculations using a least squares fit approach (see Methods).

[c]Phases were too small for pristine chemical analysis, so a representative composition from bracketing experiments was used, or measurement was normalized without contaminating elements (Sp only).

[d]Indicates starting material was layered with an equal weight proportion (50 wt.%) of pure calcite (see Methods).

[e]+ indicates the phase was visually and semi-quantitatively (EDS) identified but due to the small grain size of some phases, mass balance could not be calculated.

2.3. Analytical Techniques

2.3.1. Texture and Phase Chemistry

In order to investigate textural relationship among phases, backscattered electron images were taken of all andesite, andesite-calcite, dacite, and dacite-calcite runs using a Cameca SX100 electron microprobe at NASA Johnson Space Center in Houston, Texas and a JEOL JXA 8530F HyperProbe at Rice University, Houston, Texas.

Samples polished in epoxy were also analyzed by microprobe for phase identification based on EDS analysis and quantitative phase compositional determination using WDS analysis. A 15 kV, 10 nA electron beam was used with 1 μm spot size for silicates and 2 or 10 μm spot size for melt, depending on melt pool size, and for carbonate. Peak counting times for Si, Al, Ti, Fe, Mn, and Mg were 30 s with 10 s background counts on each, whereas for Na, K, and P, which were analyzed first to minimize potential volatility-induced migration away from the electronbeam, peak counting time was 20 s peak and 10 s background on the Cameca, and peak of 10 s with 5 s background on the JEOL. Both natural minerals and synthetic glasses were used as standards for Cameca SX100 analyses in NASA-JSC [see *Dasgupta et al*., 2013; *Mallik et al*., 2015]. EPMA analyses at JEOL JXA 8530F HyperProbe at Rice University used a natural basaltic glass (Na_2O, SiO_2, CaO, K_2O, Al_2O_3, MgO), olivine (SiO_2, FeO, MgO), rutile (TiO_2), plagioclase (Na_2O, CaO, Al_2O_3), orthoclase (K_2O), and rhodonite (MnO) as analytical standards. Multiple spot or line analyses (*n* in Tables 3–5) were collected for each phase.

2.3.2. Mass Balance and CO_2 Calculations

Mass proportions of phases present were calculated where possible based on least square minimization approach using major element oxides of analyzed phases (using representative or normalized compositions on small grains of e.g., quartz and spinel where analysis proved difficult; see Table 2) and bulk starting compositions. Calcite consumption was estimated by subtracting the modal proportion of calcite determined by mass balance calculations from the starting fraction in the system (0.5). Carbonate assimilation was then determined as the percentage of calcite consumed into the mass of silicate portion of the capsule and CO_2 calculated as 44 wt.% of that (based on 44 g CO_2 per 100 g $CaCO_3$).

3. Results

Table 2 lists modal proportions (or presence in one case) of run products and Tables (3–5) report major element composition of phases. Typical experimental textures are shown in Figure 1.

3.1. Approach to Equilibrium

Although it has been shown that carbonate reacts with melt much faster than our run durations (Table 1) [*Deegan et al*., 2010; *Jolis et al*., 2013], an approach to equilibrium and closed system were assessed in our experiments by textural (see Figure 1) and chemical evidence (lack of zoning on minerals or heterogeneities between spot analyses on a single phase, and low sum of residuals in mass balance calculations). Additionally, a set of time series (24, 48, and 96 h) experiments at low-temperature and pressure conditions (1075°C, 0.5 GPa) confirmed an experimental duration of 48 h was sufficient to ensure an approach to equilibrium between andesite and calcite based on identical mineralogy and minimal compositional difference of the resulting phases between 48 and 96 h runs and low mass balance residuals ($<$0.5). However, even with 96 h run durations, several experiments with dacitic compositions resulted in very small ($<$2–5 microns in diameter) grains for the aluminous phases such as plagioclase and spinel.

3.2. Liquid Lines of Descent: Phase Assemblage, Texture, and Chemistry

In calcite-free runs, melt and mineral phases, when present, are interspersed throughout the capsule. In calcite-bearing runs, partial assimilation leaves residual calcite at the base of the capsule, often with an interaction front rich in skarn minerals between calcite and the overlying silicate assemblage. When assimilation is high, often little to no calcite is observed in the particular cross section to which the sample was polished (near the middle of the capsule, e.g., Figure 1d). The presence of vesicles in the melts also indicates a vapor phase. These circular voids are more numerous but smaller in runs with low assimilation (Figures 1g and 1h) than in runs with very little to no calcite observed (Figure 1d).

Both magma compositions were run at constant pressure over a temperature range to identify their liquid lines of descent in a closed system (Table 2). Andesite crosses the liquidus above 1175°C at 0.5 GPa with

Table 3. Major Element Melt Composition[a]

Experiment No.	B343	B328	B334	B335	B347	B310	B369	B340	B324	B326	B325	B344B	B317	B313	B318
F^*[b]	32	54	62	83	84	100	23	57	66	93	97	99	95	100	97
n	12	20	47	15	12	37	12	6	45	6	9	99	14	17	10
SiO_2	74 (3)	66 (2)	66.9 (5)	62.4 (8)	62.6 (7)	59.7 (6)	73 (2)	69 (3)	66.9 (5)	45 (3)	38.4 (5)	37.4 (3)	37.4 (7)	38.3 (4)	39 (1)
TiO_2	1.1 (1)	1.1 (2)	0.66 (4)	1.00 (4)	0.97 (4)	0.79 (3)	1.0 (1)	0.8 (2)	0.66 (4)	0.73 (7)	0.61 (3)	0.50 (3)	0.52 (3)	0.53 (3)	0.59 (5)
Al_2O_3	13.1 (5)	15 (2)	13.0 (1)	15.4 (2)	15.7 (2)	14.1 (2)	12.7 (8)	15 (4)	13.0 (1)	11 (2)	9.6 (2)	8.76 (8)	8.7 (2)	9.0 (1)	9.8 (4)
FeO_T[c]	2.1 (8)	3.3 (9)	5.6 (1)	5.0 (3)	3.2 (4)	6.3 (1)	2 (1)	2.6 (9)	5.57 (1)	2.3 (5)	1.64 (7)	0.23 (4)	2.3 (5)	1.94 (6)	2.0 (1)
MnO	0.04 (2)	0.08 (4)	0.12 (3)	0.12 (3)	0.12 (4)	0.14 (3)	0.03 (2)	0.03 (3)	0.13 (4)	0.09 (4)	0.09 (3)	0.04 (2)	0.07 (3)	0.06 (3)	0.10 (3)
MgO	0.74 (1)	2 (1)	3.71 (6)	3.5 (2)	4.4 (2)	6.5 (1)	1.1 (6)	1.3 (3)	3.71 (6)	4 (2)	3.6 (2)	4.18 (7)	5.5 (8)	4.26 (9)	4.3 (1)
CaO	1.6 (3)	5 (1)	7.5 (1)	6.6 (3)	7.2 (3)	7.6 (1)	1.3 (8)	3 (2)	7.5 (1)	31 (2)	42.0 (1)	45.8 (2)	42.3 (4)	42.7 (4)	40.3 (9)
Na_2O	4.6 (6)	4.3 (7)	3.3 (7)	3.9 (1)	3.9 (1)	3.31 (8)	5.3 (3)	5.2 (9)	0.9 (7)	3.7 (5)	2.7 (1)	2.10 (8)	2.1 (1)	2.12 (7)	2.6 (2)
K_2O	3.0 (1)	2.1 (4)	1.38 (8)	1.85 (9)	1.62 (9)	1.39 (5)	3.8 (3)	2.9 (5)	1.38 (8)	1.6 (3)	1.10 (6)	0.89 (4)	0.89 (6)	0.88 (5)	1.20 (7)
P_2O_5	0.23 (9)	0.3 (1)	0.27 (8)	0.30 (9)	0.26 (6)	0.24 (7)	0.16 (5)	0.2 (1)	0.27 (8)	0.24 (4)	0.20 (5)	0.15 (6)	0.16 (6)	0.17 (5)	0.18 (6)
Sum[d]	100 (3)	100.0 (9)	100.0 (3)	100.0 (7)	100.0 (4)	100.0 (9)	100 (2)	100.0 (8)	100.0 (3)	100 (3)	100.0 (7)	100.0 (5)	100.0 (8)	100.0 (8)	100 (1)
Est. H_2O+CO_2[e]	2 (3)	0.0 (9)	9.0 (3)	1.8 (7)	0.7 (4)	5.9 (9)	3 (2)	0.0 (8)	9.9 (3)	7 (3)	11.7 (7)	11.0 (5)	10.7 (8)	12.6 (8)	14 (1)
Mg#[f]	40 (12)	51 (10)	59.7 (6)	57 (2)	71 (3)	68.8 (6)	60 (14)	47 (8)	59.7 (6)	79 (5)	89.9 (9)	109.1 (5)	90 (5)	91.2 (6)	93 (1)
CaO/Al_2O_3[g]	0.12 (2)	0.3 (1)	0.63 (1)	0.44 (2)	0.46 (2)	0.57 (1)	0.7 (2)	0.2 (2)	0.63 (1)	3.0 (5)	4.93 (9)	5.87 (6)	5.4 (1)	5.41 (7)	4.8 (3)
NBO/T[h]	0.02 (4)	0.064 (5)	0.051 (8)	0.093 (9)	0.116 (4)	0.12 (7)	0.03 (1)	0.036 (3)	0.03 (2)	0.064 (5)	0.71 (8)	1.19 (1)	1.41 (1)	1.29 (6)	1.25 (1)
π^*[i]	0.15 (3)	0.198 (8)	0.206 (7)	0.209 (6)	0.251 (3)	0.17 (2)	0.13 (2)	0.092 (8)	0.12 (2)	0.198 (8)	0.82 (9)	1.29 (2)	1.413 (1)	1.35 (2)	1.33 (1)

Experiment no.	B382A	B377	B380A	B392	B381	B380B
F^*[b]	39	+	100	52	49	52
N	8	14	47	20	11	15
SiO_2	78 (3)	76 (2)	67.2 (4)	68 (3)	76.8 (8)	72.3 (8)
TiO_2	0.33 (7)	0.9 (2)	0.70 (4)	0.3 (2)	0.8 (1)	0.76 (4)
Al_2O_3	11 (1)	12 (1)	14.8 (2)	17 (3)	10.9 (3)	12.4 (4)
FeO_T[c]	1.6 (4)	0.9 (4)	5.3 (1)	3 (1)	1.1 (1)	3.5 (2)
MnO	0.03 (3)	0.02 (2)	0.07 (3)	0.03 (2)	0.04 (3)	0.06 (2)
MgO	0.3 (2)	0.3 (2)	1.72 (5)	0.6 (6)	0.18 (2)	0.53 (6)
CaO	1.0 (5)	0.7 (4)	4.3 (1)	2 (2)	0.6 (2)	2.7 (2)
Na_2O	3.9 (4)	4.7 (5)	3.5 (1)	6.0 (1)	4.8 (2)	4.5 (1)
K_2O	3.6 (3)	4.9 (2)	2.19 (8)	4 (1)	4.8 (2)	3.0 (1)
P_2O_5	0.07 (7)	0.11 (8)	0.21 (7)	0.2 (3)	0.05 (5)	0.20 (4)
Sum[d]	100.0 (9)	100.0 (7)	100.0 (4)	101 (1)	100.0 (5)	100.0 (6)
Est. H_2O+CO_2[e]	3.8 (9)	1.5 (7)	4.4 (4)	1 (1)	1.3 (5)	0.8 (6)
Mg#[f]	22 (6)	40 (14)	36.5 (1)	20 (10)	30 (10)	21 (2)
CaO/Al_2O_3[g]	0.09 (4)	0.06 (3)	0.305 (8)	0.1 (1)	0.06 (1)	0.22 (1)
NBO/T[h]	0.039 (8)	0.03 (1)	0.027 (4)	0.00 (3)	0.034 (1)	0.034 (3)
π^*[i]	0.08 (1)	0.085 (9)	0.150 (3)	0.00 (5)	0.083 (5)	0.114 (4)

[a]All data are in wt.% on a volatile-free basis with error ($\pm 1\sigma$ standard deviation) for *n*-number of analyses given in parentheses to the last digit provided, e.g., 74(3) is 74 $\pm$ 3 wt.%. Calcite (wt.%) indicates if the run contained calcite (in equal weight proportion—50:50—to the Starting Melt—Basalt, Andesite, or Dacite).

[b]F^* is the melt fraction (in percent) normalized to the sum of all silicates present in the capsule as determined by mass balance (See Table 2).

[c]FeO_T indicates all iron assumed to be Fe^{2+}.

[d]Sum gives the total of all major elements normalized on a volatile-free basis.

[e]Est. H_2O+CO_2 is the total volatile content of the melt as determined by deficit from 100 wt.% in EMP analyses.

[f]Mg# is the proportion of Mg to Fe (Mg/(Mg + Fe) in moles.

[g]CaO/Al_2O_3 is the wt.% ratio used to determine if a melt is ultracalcic (>1).

[h]NBO/T is the Non-Bridging Oxygen to Tetrahedra ratio as calculated by the following formula: absolute value of (4*T-2*O)/T where T is the sum of Si, Al, Fe, Ti, P in moles, after *Brooker et al*. [2011] (see text).

[i]π^* is another way to determine melt polymerization using weighted element proportions as given by *Shishkina et al*. [2014] by the following formula: (Ca+0.8*K+0.7*Na+0.4*Mg+0.4*Fe)/(Si + Al), again in moles (see text).

increasing proportions of plagioclase, spinel, cpx, and opx with decreasing temperature. The dacite liquidus lies lower, at <1100°C at 0.5 GPa (confirmed with alphaMELTS) [*Ghiorso and Sack*, 1995], below which clinopyroxene, more Na-rich feldspar, spinel, ilmenite, and quartz can also be present.

In calcite-free experiments, clinopyroxene, stable until the liquidus, largely classifies as diopside with little deviation between those formed from andesite or from dacite (Table 4). Orthopyroxene is present at low temperatures in andesite runs, but lacking in the dacite-derived assemblages. In andesite experiments, feldspar is anorthitic ($An_{\geq 56}$; Table 5), and lower in abundance than in dacite experiments at their respective lowest temperatures (Table 2). Occasionally with corundum cores due to the sluggish diffusivity of aluminum, hercynite is present at low temperature in dacite runs, but is more of a spinel-hercynite solid solution in andesite runs (supporting information Table S1). With low melt fractions of parental andesite and dacite, quartz, and in two cases, trace ilmenite is also present (Table 2 and supporting information Table S1).

Table 4. Clinopyroxene and Wollastonite Compositions[a]

Experiment No.	B343	B328	B334	B335	B347	B369	B340	B324	B324	B326	B325	B325	B325
Phase[b]	Cpx	Cpx	Cpx	Cpx	Cpx	Cpx	Cpx	Wo	Cpx	Wo	Cpx	Wo	Cpx
n	2	6	9	6	3	6	7	5	4	7	7	7	7
SiO_2	57 (2)	53.6 (1)	53 (1)	52 (1)	53.6 (4)	51 (2)	53 (1)	51 (1)	52.8 (5)	50.0 (9)	48 (1)	49.2 (5)	50.2 (9)
TiO_2	1 (1)	0.6 (2)	0.33 (8)	0.4 (2)	0.5 (2)	0.5 (1)	0.6 (2)	0.08 (3)	0.6 (2)	0.07 (2)	0.51 (7)	0.07 (3)	0.33 (6)
Al_2O_3	3 (1)	0.8 (5)	2.0 (8)	0.9 (4)	1.0 (5)	1.6 (1)	0.7 (3)	0.04 (3)	1 (1)	0.05 (2)	8 (1)	0.07 (2)	8 (1)
FeO_T[c]	10.8 (2)	10 (2)	5.9 (5)	7.3 (9)	8 (1)	10 (3)	9 (1)	1.5 (4)	8 (2)	0.39 (5)	1.9 (5)	0.48 (6)	2.2 (4)
MnO	0.24 (3)	0.26 (1)	0.3 (2)	0.3 (3)	0.21 (7)	0.2 (1)	0.21 (8)	0.13 (6)	0.3 (1)	0.07 (4)	0.03 (4)	0.08 (3)	0.05 (3)
MgO	13.3 (6)	16 (2)	18.1 (5)	17 (1)	18 (1)	13 (2)	15 (3)	0.49 (8)	18 (1)	0.8 (1)	13.7 (7)	0.79 (5)	14.0 (7)
CaO	14 (1)	18 (1)	18.7 (3)	18 (1)	17.3 (6)	21 (2)	20 (3)	45.7 (5)	18.0 (8)	46.4 (2)	25.0 (7)	46.3 (3)	24.7 (2)
Na_2O	1.1 (3)	0.5 (2)	0.37 (8)	0.38 (7)	0.40 (9)	0.7 (2)	0.44 (8)	0.005 (8)	0.6 (1)	0.01 (1)	0.23 (4)	0.01 (1)	0.42 (5)
K_2O	0.42 (6)	0.06 (3)	0.04 (3)	0.033 (1)	0.05 (2)	0.1 (1)	0.05 (4)	0.02 (2)	0.08 (7)	0.008 (5)	0.02 (2)	0.01 (1)	0.01 (1)
P_2O_5	0.07 (5)	0.1 (1)	0.04 (6)	0.09 (7)	0.03 (3)	0.3 (5)	0.1 (1)	0.06 (5)	0.06 (5)	0.02 (4)	0.03 (3)	0.03 (5)	0.02 (3)
Sum	101.5 (8)	99.5 (6)	99 (1)	96.5 (8)	98.9 (3)	98 (1)	98.8 (4)	99 (1)	99.4 (9)	97.8 (9)	97.7 (8)	97.0 (6)	100.2 (4)
En[d]	45 (3)	47 (5)	52 (1)	50 (3)	51 (2)	38 (6)	43 (8)	1.5 (2)	50 (3)	2.2 (4)	42 (2)	2.3 (1)	42 (1)
Fs	20 (−)	16 (4)	9.5 (7)	12 (2)	13 (2)	16 (5)	14 (2)	2.4 (7)	13 (2)	0.7 (−)	3 (−)	0.8 (−)	4 (−)
Wo	35 (3)	37 (2)	38.5 (9)	38 (3)	36 (−)	46 (5)	43 (7)	96.1 (9)	37 (2)	97.1 (3)	55 (2)	96.9 (2)	54 (−)
En + Fs[e]	64 (−)	61.0 (6)	59.3 (2)	59.7 (8)	62.4 (3)	53 (2)	55 (1)		61.4 (5)		42.5 (3)		43.4 (−)
Wo	32 (−)	37.3 (−)	38.5 (−)	39.3 (−)	36.5 (−)	45.2 (1)	44 (−)		37.4 (−)		47.3 (−)		46.6 (−)
CaTs	4 (2)	1.7 (9)	2.2 (2)	1 (1)	1.1 (5)	2 (3)	1 (2)		1.2 (7)		10.2 (4)		10 (−)

Experiment no.	B382A	B377	B392	B392	B381	B381	B380B	B380B
Phase[b]	Cpx	Cpx	Wo	Cpx	Wo	Cpx	Wo	Cpx
n	1	4	4	4	4	7	3	4
SiO_2	55.49	51.8 (1)	48.9 (7)	52 (1)	50.5 (6)	53.1 (9)	49.7 (7)	52 (2)
TiO_2	0.39	0.7 (5)	0.07 (5)	0.6 (1)	0.2 (1)	1.6 (7)	0.13 (2)	0.7 (3)
Al_2O_3	1.89	0.5 (2)	0.07 (8)	0.31 (4)	1 (2)	0.8 (9)	0.2 (2)	1.3 (8)
FeO_T[c]	8.57	13 (4)	1.4 (3)	14 (2)	2.5 (6)	11 (3)	1.3 (2)	10 (5)
MnO	0.10	0.3 (1)	0.14 (8)	0.3 (2)	0.07 (3)	0.2 (1)	0.08 (1)	0.14 (7)
MgO	13.10	12 (3)	0.2 (2)	10 (2)	0.6 (2)	11 (2)	0.26 (3)	13 (4)
CaO	19.88	18 (1)	45.1 (6)	20 (2)	44 (1)	21 (2)	46.8 (1)	22 (1)
Na_2O	0.83	0.8 (3)	0.03 (2)	1.9 (9)	0.2 (3)	1.1 (2)	0.03 (2)	0.5 (2)
K_2O	0.23	0.12 (3)	0.03 (1)	0.06 (2)	0.04 (2)	0.3 (3)	0.001 (2)	0.07 (3)
P_2O_5	0.16	0.17 (8)	0.03 (2)	0.2 (2)	0.04 (3)	0.1 (1)	0.03 (3)	1 (1)
Sum	100.63	98.5 (3)	96 (1)	99.4 (5)	99.7 (9)	100.3 (4)	99 (1)	100 (1)
En[d]	44	40 (2)	97.0 (6)	46 (2)	94 (1)	48 (3)	97.1 (4)	47 (3)
Fs	41	37 (7)	0.6 (5)	30 (4)	2 (−)	33 (4)	0.7 (−)	37 (10)
Wo	15	23 (7)	2.4 (5)	24 (5)	4 (−)	19 (6)	2.2 (4)	16 (9)
En + Fs[e]	54 (2)	59 (2)		54 (−)		51 (1)		52.1 (6)
Wo	44 (−)	40 (−)		46 (−)		48 (−)		46.5 (−)
CaTs	2 (5)	1 (3)		0 (1)		1 (2)		1.4 (9)

[a]All data are in wt.% with error ($\pm 1\sigma$ standard deviation) for *n*-number of analyses given in parenthesis to the last digit provided; e.g., 57(2) is 57 ± 2 wt.%.
[b]Indicates phase, clinopyroxene (Cpx,) or wollastonite (Wo).
[c]FeO_T indicates all iron assumed to be Fe^{2+}.
[d]Refers to ternary end-members Enstatite ($Mg_2Si_2O_6$), Ferrosilite ($Fe_2Si_2O_6$), and Wollastonite ($Ca_2Si_2O_6$), respectively, calculated based on cation proportions, with $\pm 1\sigma$ standard deviation based on *n*-analyses given in parentheses to the last digit provided; e.g., 45(3) is 45 ± 3%.
[e]Gives ternary end-members now taking into account Ca-Tschermak (CaTs) component ($CaAlAlSiO_6$) in clinopyroxene (Cpx) with ± error (calculated by Monte Carlo simulation using compositional standard deviation of replicate analyses of Cpx within a run) in parentheses where (−) indicates negligible error to the last digit provided; e.g., 61.0(6) is 61.0 ±0.6%.

The melts above the liquidus are andesite and dacite, respectively. At lower melt fractions, they are more siliceous, even becoming rhyolitic (Figure 2). With increasing temperature, all melts become more magnesian and less alkalic, whereas calcium, aluminum, and iron show little variation (Table 3).

3.3. Melt-Calcite Reactions: Phase Assemblage, Texture, and Chemistry

With both starting melts, the presence of calcite increases the liquidus of the system to higher temperatures. With andesite it shifts to >1200°C at 0.5 GPa. The addition of calcite to dacite at 0.5 GPa has a much more drastic effect on raising the liquidus temperature. Melt fraction (*F**, melt fraction calculated on calcite-free basis) is only ~66% at 1100°C with calcite interaction (Table 3, Figure 3).

Clinopyroxene is stable to higher temperatures at 0.5 GPa in calcite-bearing runs than runs performed along liquid lines of descent (Table 2). The clinopyroxenes are consistently diopsidic in all runs, shifted only slightly toward ferrosilite-hedenbergite in the clinopyroxene quadrilateral with increasing temperature (Figure 4). Clinopyroxenes formed in runs with high calcite consumption additionally show an elevated Ca-Tschermak (CaTs) component (Table 4).

Table 5. Feldspar Compositions[a]

Experiment No.	B343	B328	B334	B335	B347	B369	B340	B324	B381
n	1	1	1	6	6	1	1	2	1
SiO_2	54.63	59.71	58.67	53.5 (5)	48 (3)	49.62	65.25	56.9 (7)	61.94
TiO_2	0.38	0.46	0.76	0.09 (4)	0.17 (8)	0.27	0.19	0.16 (2)	0.15
Al_2O_3	26.28	22.50	15.41	27.6 (3)	30 (2)	26.95	20.1	24.4 (9)	22.9
FeO_T[b]	1.87	1.55	4.50	0.7 (1)	0.7 (3)	4.04	1.23	0.95 (1)	0.44
MnO	0.02	0.06	0.10	0.01 (1)	0.02 (2)	0.10	0.00	0.03 (4)	0.01
MgO	0.77	0.67	5.26	0.2 (1)	1.1 (6)	6.68	1.81	0.21 (4)	0.02
CaO	8.39	7.78	7.60	11.0 (4)	13 (1)	5.61	3.72	8.2 (3)	5.16
Na_2O	4.63	5.06	2.5	4.7 (3)	3.0 (5)	5.09	7.80	6.2 (3)	7.02
K_2O	0.61	0.99	1.39	0.36 (3)	0.2 (2)	0.51	1.23	0.59 (1)	1.32
P_2O_5	0.01	0.16	0.26	0.04 (4)	0.07 (2)	0.78	0.14	0.07 (3)	0.00
Sum	97.59	98.95	96.46	98.2 (6)	97 (1)	99.65	101.52	98 (2)	98.99
An[c]	68	56	71.2	77 (2)	78 (8)	58	62	73 (1)	42
Ab	32	40	21	22 (2)	18 (9)	21	35	25 (2)	52
Or	0	4	7.7	1 (1)	4 (2)	21	3	2 (1)	6

[a]All data are in wt.% with error ($\pm 1\sigma$ standard deviation) for *n*-number of analyses given in parentheses to the last digit provided, e.g., 53.5 (5) is 53.5 ± 0.5 wt.%.

[b]FeO_T indicates all iron assumed to be Fe^{2+}.

[c]Refers to ternary end-members Anorthite (An, $CaAl_2Si_2O_8$), Albite (Ab, $NaAlSi_3O_8$), and Orthoclase (Or, $KAlSi_3O_8$), respectively, calculated based on cation proportions, with $\pm 1\sigma$ standard deviation based on *n*-analyses given in parentheses to the last digit provided; e.g., 77(2) is 77 ± 2%.

Wollastonite is present in all runs above 1075°C with the andesite starting melt, even beyond clinopyroxene exhaustion (>1175°C), and in all dacite runs (900–1100°C) increasing in abundance while clinopyroxene declines with increasing temperature (Table 2).

With higher percent assimilation in andesite-calcite reactions, feldspar becomes more anorthitic plagioclase (An_{58-73}) until its exhaustion above 1150°C. In dacite-calcite reactions, small plagioclase grains were present from 900 to 1000°C and, though reliable WDS analyses were not feasible owing to small grain sizes, seem to be more albite-than anorthite-rich (Table 5 and Figure 5).

Some minor to trace phases are also present at low temperatures (Table 2 and supporting information Table S1). Similar to calcite-free runs, spinel-hercynite solid solution is present consistently in dacite-calcite runs and up to 1100°C in andesite-calcite runs. Additionally, quartz exists throughout the capsule in conjunction with highly siliceous melts, and one run contained a few interspersed small ilmenite grains. Scapolite appears in its calcic carbonate-bearing end-member (meionite) in midtemperature range (1100–1150°C) in andesite runs over a pressure range of 0.5–1.0 GPa.

3.4. Calcite-Contaminated Melts

At low melt fraction, with little calcite ingested, melts fall into a similar Total Alkali-Silica (TAS) field as calcite-free melts (Figure 3). Here, they most nearly match calcite-free trends in each oxide (Table 3), especially in dacite-calcite reactions. With increasing temperature, and thus melt fraction, and decreasing calcite in the residuum (Table 2), melts in andesite-calcite runs become increasingly silica-undersaturated—foiditic (≤45 wt.% SiO_2, $T > 1100$°C)—while increasing the temperature of dacite-calcite melts has an exceedingly diminished effect on their elevated—rhyolitic to dacitic (67–79 wt.% SiO_2 without calcite, 72–77 wt.% SiO_2 with calcite)—silica content (Figure 2). This trend is exactly opposite to the calcium trend (Figure 3a), reaching a maximum in all experiments above the liquidus of the andesitic starting material (>45 wt.% CaO, on a volatile-free basis; Table 3) and increasing negligibly across the dacite liquidus (0.6–2.7 wt.% CaO from 1000 to 1100°C). It is unsurprising then that contaminated andesite data deviate the most from calcite-free calcium (<10 wt.% CaO) and silica (≥60 wt.% SiO_2) compositions (Figure 3a) and are significantly ultracalcic (≤5.9 CaO/Al_2O_3 wt.% ratio; Table 3). Alumina and TiO_2 both mirror silica on a much smaller scale in andesite runs (∼13–15 wt.% Al_2O_3 without calcite, ≥8.7 wt.% Al_2O_3 with calcite and 1.1–0.98 wt.% TiO_2 without calcite, 1.0–0.50 wt.% TiO_2 with calcite; Table 3), but alumina slightly increases in dacite experiments (∼11–15 wt.% Al_2O_3 without calcite, 11–17 wt.% Al_2O_3 with calcite) with increasing Al-bearing mineral abundance (Table 2), while titanium is nearly identical (Table 3). Magnesium is relatively minor (≤5.5 wt.% MgO) and shows an insignificant increase with andesite, while it is nearly nonexistent (<1 wt.% MgO; Table 3) and fluctuates in dacite-calcite runs. Iron is also affected by the mineral phases present, showing a peak near

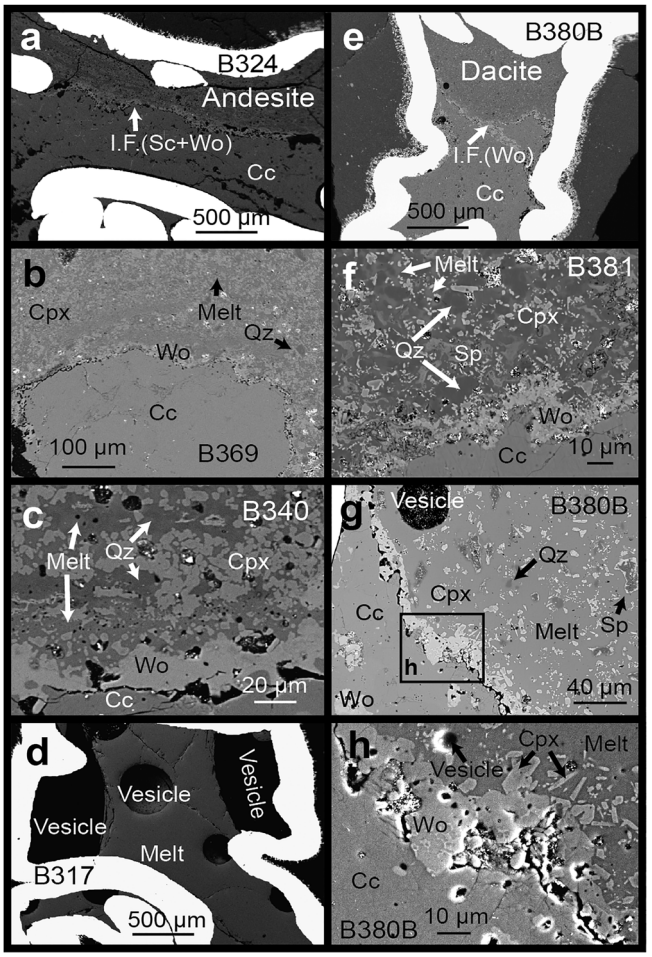

Figure 1. Back-Scattered Electron (BSE) images showing textures of experimental run products of melt-calcite interaction. (a) Andesite-calcite reaction at 0.5 GPa and 1100°C, with interaction front (I.F.), which is largely composed of wollastonite (Wo) and scapolite (Sc), separating silicate melt and crystals in the top half and residual calcite (Cc) in the lower half. (b) Lowest temperature and pressure (1050°C, 0.5 GPa) andesite-calcite crystallized quartz (Qz) in addition to silicate phases present in most runs (clinopyroxene, Cpx; Spinel, Sp; and melt) and clearly shows the wollastonite-rich layer interaction front. (c) Slightly higher temperature (1075°C, 0.5 GPa) andesite-calcite interaction has similar phase assemblage with higher melt proportion. (d) High-temperature andesite-calcite run (0.5 GPa, 1200°C) contains minor wollastonite and residual calcite, clearly dominant in melt and large vesicles. (e) High-temperature (0.5 GPa, 1200°C) dacite-calcite interaction shows the overall silicate-carbonate layered texture of most experiments with a wollastonite interaction front. (f) At 1000°C, 0.5 GPa, dacite and calcite react little, with many silicate phases, and skarn-like wollastonite at the interface. (g) Zooming onto the interface shows residual calcite, and silicate melt containing quartz, clinopyroxene and spinel (Sp) grains and a vesicle. The box indicates the view shown in (h). Closer imagery shows wollastonite proximal to residual carbonate like an exoskarn, whereas clinopyroxene crystals are present in the contaminated melt similar to an endoskarn.

high-temperature andesite-calcite experiments ($\leq$6.0 wt.%, FeO_T, maximum at 1100°C) above exhaustion of spinel. Again, little change is evident in dacite-calcite experiments (1.1–3.5 wt.% FeO_T, maximum at 1100°C). Overall, alkalis are diluted with raising temperature, dropping below calcite-free values in andesite-calcite reacted melts (2.2–7.6 wt.% $Na_2O + K_2O$ calcite-free versus 2.9–9.1 wt.% calcite-contaminated, maximum at 1075°C) and raising above calcite-free values in dacite-calcite melts (5.6–9.6 wt.% $Na_2O + K_2O$ calcite-free versus 7.6–10.0 wt.% calcite-contaminated, maximum at 1000°C, 0.5 GPa).

3.5. Calcite Saturation in Contaminated Melt

Overall, the amount of calcite assimilated by the magma increases with increasing melt fraction, such that at identical pressure-composition condition, the higher temperature consumes more calcite (Figure 3b). Near-liquidus andesite consumes the most at ~65% assimilation. The maximum with dacite is ~18%. As discussed above, as assimilation increases, the contaminated melts become more calcium-rich, diluting silica in the process (Figure 3a). Andesite melts become ultracalcic (CaO/Al_2O_3 wt.% ratio $\gg$ 1) whereas low assimilation keeps dacite melt dominant in Al_2O_3 over CaO (Table 3).

Though some alkali loss during analysis might have occurred (see Methods), a maximum melt volatile content can be estimated by EMPA difference (from total of 100 wt.%; Table 3). Volatile content increases with assimilation in andesite-calcite runs (as much as >10 wt.% $H_2O + CO_2$ at >1125°C at 0.5, 1200°C at 0.8 and 1.0 GPa), but remains exceedingly small (~1 wt.% $H_2O + CO_2$) in calcite-contaminated dacite melts, even more so than the hydrous dacite melts alone (~1.5–4.4 wt.% H_2O).

4. Discussion

4.1. Melt-Calcite Reactions

Time series experiments (at 24, 48, and 96 h) convey a first-order indication of reaction time between andesite melt and calcite as the system approaches equilibrium at low pressure and temperature (0.5 GPa,

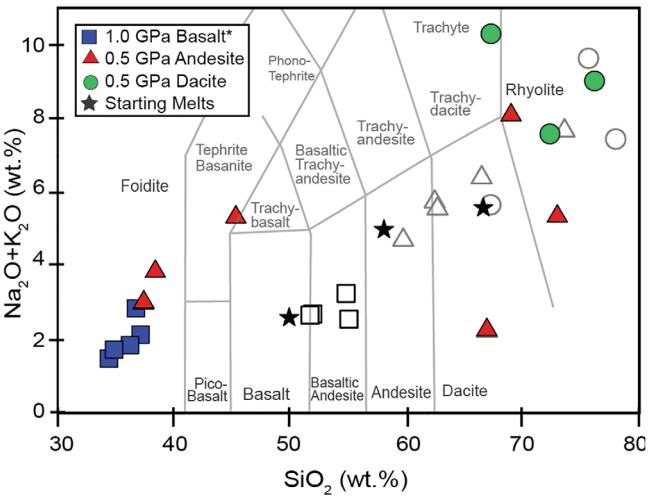

Figure 2. Total Alkali-Silica (TAS) classifications of experimental melts in wt.% based on a volatile-free normalization. Starting melt compositions (see Table 2 and *Carter and Dasgupta* [2015]) are given as stars. Liquid line of descent (LLD) melt compositions are open symbols (square = basalt* from *Carter and Dasgupta* [2015] at 1.0 GPa, and triangle = andesite and circle = dacite from this study at 0.5 GPa). Closed symbols, the same shape as the LLD (blue = basalt, red = andesite, green- = dacite), represent contaminated melts in melt-calcite runs at 0.5 GPa.

1075°C). Although similar in modal abundance, after only 24 h some of the oxides have not had time to fully diffuse, producing two unique clinopyroxene compositions—a calcium-rich composition at the interface near wollastonite, and hedenbergite near the top of the capsule—and an aluminosilicate phase. Extending the duration to 48 h permits clinopyroxene equilibration into a single diopside composition, and a silica-poor magnesioferric aluminous spinel. This assemblage is notably similar in mineralogy (see Table 2) and alike in composition to the run performed at identical conditions for 96 h (e.g., clinopyroxene ternary end-members $Fs_{14}Wo_{42}En_{44}$ after 48 h, $Fs_{14}Wo_{43}En_{43}$ after 96 h, where Fs = Ferrosilite, Wo = Wollastonite, En = Enstatite), confirming that after 48 h the system approached equilibrium. On the other hand, the melt composition, on a volatile-free basis, changes little with increasing run time such that the 24 and 48 h melts are nearly indistinguishable from the composition given in Table 3 (the 96 h melt) within 2σ. Additionally, mass balance calculations return similar calcite consumption estimates for incrementally longer experiments (Table 2). The conclusion is that calcite consumption and carbonate-melt reactivity are fairly rapid, as corroborated by previous time-series experiments [*Deegan et al*., 2010; *Jolis et al*., 2013], even at low melt fraction, but mineral equilibration is slower.

Using calculated mineral modal abundances where possible (Table 2), the addition of calcite to andesite versus dacite systems shows that in general the consumption of calcite can either generate or consume melt and cpx at low pressures (0.5 GPa). Andesite-calcite experiments with the addition of quartz at low temperature generate similar mineral assemblages to basalt-calcite, at slightly lower temperatures due to a slight drop in liquidus temperature [*Carter and Dasgupta*, 2015]. At 0.5 GPa, the mineral phases present are clinopyroxene, plagioclase, scapolite, ± quartz at temperatures just below the liquidus (1100–1150°C), and a small proportion (≤4 wt.%, Table 2) of wollastonite (1100–1200°C). The andesite-calcite reactions largely consume calcite (Cc), plagioclase (Plag) and orthopyroxene (Opx) to produce clinopyroxene (Cpx) in addition to spinel (Sp) and some CO_2 at low temperatures. At higher temperatures clinopyroxene is instead a reactant producing wollastonite (Wo), melt, and CO_2. In low-temperature dacite-calcite reactions, wollastonite replaces clinopyroxene, plagioclase, and calcite, whereas at high-temperature wollastonite, clinopyroxene, and plagioclase replace melt and calcite. These run products are comparatively clinopyroxene-poor, replaced by a more significant wollastonite modal abundance (up to ~28 wt.% of silicates). Low temperature assemblages also contain trace quartz ± ilmenite interspersed in the rhyolitic glass.

At temperatures with lower melt fractions (F^* = 53%, 1075°C), calcite consumption by andesite leads to production of clinopyroxene and an increased abundance of melt:

$$0.41\ Opx + 0.75\ Plag + 0.01\ Cc \rightarrow 0.11\ Sp + 0.06\ Cpx + 1.00\ Melt\ (+CO_2) \quad (1)$$

Although coefficients were calculated on a volatile-free basis, CO_2 is a product of this reaction. For every 1.00 g of melt produced, this reaction releases 0.004 g total CO_2 (in melt + vapor). In contrast, at low temperature (F^* = 52%, 900°C) dacite melt reacts with calcite to produce wollastonite and .0018 g CO_2 per 1.00 g of melt:

$$2.67\ Plag + 0.21\ Cpx + 0.04\ Cc \rightarrow 0.07\ Il + 1.22\ Qz + 0.50\ Sp + 0.13\ Wo + 1.00\ Melt\ (+CO_2) \quad (2)$$

At higher temperatures (1100°C), trace wollastonite appears and trace scapolite in andesite-calcite reaction can sequester a negligible portion (0.025%) of the 0.26 g of CO_2 released:

$$0.65\ Opx + 0.43\ Plag + 0.59\ Cc \rightarrow 0.28\ Sp\ 0.07\ Cpx + 0.01\ Sc + 0.01\ Wo + 1.00\ Melt\ (+CO_2) \quad (3)$$

At supraliquidus conditions according to its LLD (1200°C), andesite-calcite interaction generates melt, wollastonite and 0.51 g CO_2 per 1.00 g of melt:

$$1.15\ Cc \rightarrow 0.15\ Wo + 1.00\ Melt\ (+CO_2) \quad (4)$$

Dacite, above its calcite-free liquidus (1100°C), reacts with calcite, producing mostly clinopyroxene and wollastonite with 0.20 g of CO_2 per 1.00 g of melt:

$$1.00\ Melt + 0.46\ Cc \rightarrow 0.26\ Sp + 0.05\ Plag + 0.15\ Cpx + 1.00\ Wo\ (+CO_2) \quad (5)$$

The difference between reactions (1) and (2), and (4) and (5) clearly displays the largest difference in run products as the starting melt becomes more silicic. Assimilation is marginally more significant with andesite than it was with basalt (65 versus 48% assimilation at 0.5 GPa, 1200°C, discussed below, *Carter and Dasgupta* [2015], Figure 3b), with the most dominant product being contaminated melt, in conjunction with the stability of calc-silicate minerals like wollastonite and scapolite. In contrast, dacite-calcite interaction primarily results in mineralization, consuming melt. Here, the majority of consumed calcium is bound in wollastonite, ± clinopyroxene, ± plagioclase, reminiscent of skarn mineralogy.

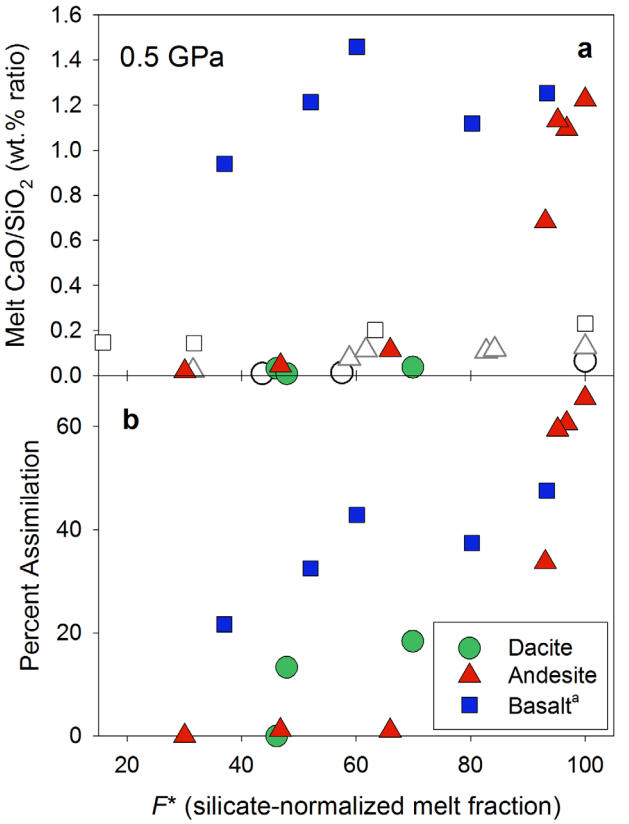

Figure 3. (a) Calcium-oxide over silica ratios (in volatile-free wt.%) of experimental melts as a function of melt fraction normalized to the silicate fraction of run products (calcite-free; *F**, see Table 3) at 0.5 GPa. Closed symbols represent calcite-contaminated melts (red triangle = andesite, green circle = dacite), and open symbols represent the liquid line of descent (LLD) of the starting compositions. [a]For comparison basalt and basalt-calcite (open and blue square symbols, respectively) have been plotted from *Carter and Dasgupta* [2015]. (b) Percent assimilation (amount of calcite consumed over silicate proportion of the capsule, as determined by mass balance, see Methods) at 0.5 GPa as a function of *F** with identical symbols to graph A, but only melt-calcite experiments plotted.

4.2. Comparison Between Experimental and Natural Skarn Mineralogy

Skarnification is a relatively low-temperature (≤500–700°C peak) metasomatic process by which fluids exsolving from the intruding magma and/or percolating into the hydrothermal system from meteoric or groundwater sources can exchange elements with the carbonate wall rock, decarbonating and leaving a calc-silicate residuum [*Einaudi et al.*, 1981; *Einaudi and Burt*, 1982b; *Meinert*, 1992, 2016; *Meinert et al.*, 2005]. Skarns are typically zoned from pluton to marble (carbonate) with more igneous textures in proximity to the intrusion—the endoskarn—grading to calc-silicate mineralogy (for the most part clinopyroxene and garnet, with or without wollastonite, vesuvianite, or phlogopite among other minor phases) in the exoskarns [e.g., *Meinert*, 1992; *Meinert et al.*, 2005a; *Rosen et al.*, 2005]. This zonation is similar to the texture observed in dacite-calcite and low temperature andesite-calcite experiments (Figure 1), wherein wollastonite lines the calcite-silicate interaction front, while diopside is in the igneous half of the capsule, which also hosts typical felsic crystals like feldspar and quartz.

Experimental feldspars are plagioclase solid solution, similar to those from

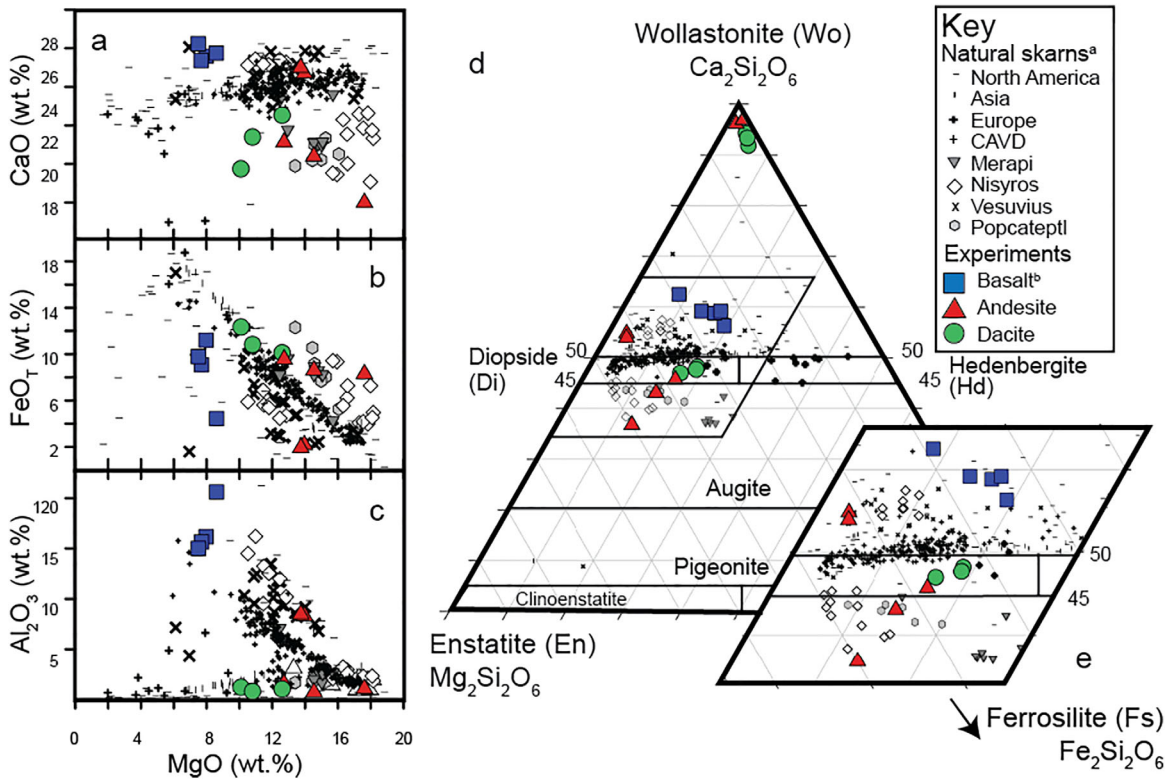

Figure 4. (a–c) Graphs depict the calcium, total iron (FeO + Fe_2O_3), and aluminum oxide concentrations, respectively, of clinopyroxene in experiments from this study (open symbols from LLD runs, and closed from 0.5 GPa calcite-bearing runs, with green circle = dacite and red triangle = andesite starting melts and darker shades representing increasing pressure from 0.5 to 0.8 to 1.0 GPa) and a past study (blue squares = basalt[b]) [*Carter and Dasgupta*, 2015] as well as natural skarns as a function of magnesium content, all in wt.%. Natural skarn data are from: North America [*Brown and Essene*, 1985; *Brown et al.*, 1985; *Meinert*, 1987; *Ray and Webster*, 1997; *Dyer et al.*, 2011; *Rasmussen et al.*, 2011]; Asia [*Wenzel*, 2002; *Groppo et al.*, 2013]; Eastern Europe [*Pertoldová et al.*, 2009]; and several volcanic centers of interest: Colli Albani Volcanic District (CAVD) [*Federico and Peccerillo*, 2002; *Gaeta et al.*, 2006; *Gozzi et al.*, 2014]; Merapi, Indonesia [*Chadwick et al.*, 2007, 2013]; Nisyros, Greece [*Spandler et al.*, 2012]; Vesuvius, Italy [*Fulignati et al.*, 2000; *Pascal et al.*, 2009]; and Popocatepetl, Mexico [*Sosa-Ceballos et al.*, 2014]. (d) Ternary diagram with overlain pyroxene quadrilateral on which experimental clinopyroxene and wollastonite from Table 4 are plotted as a function of end-members Enstatite ($Mg_2Si_2O_6$), Ferrosilite ($Fe_2Si_2O_6$), and Wollastonite ($Ca_2Si_2O_6$), respectively, determined by stoichiometric cation proportions. Data and symbols as in Figures 4a–4c, depicted in the legend. (e) Zooming into the diopsidic part of the quadrilateral as represented by the parallelogram in ternary graph d, shows the similarity between skarn and experimental clinopyroxene compositions.

most natural skarns due to the high concentration of calcium in the system (Figure 5) [e.g., *Pan et al.*, 1994; *Fulignati et al.*, 2000; *Wenzel*, 2002; *Piochi et al.*, 2006; *Aleksandrov*, 2011; *Dyer et al.*, 2011; *Spandler et al.*, 2012; *Groppo et al.*, 2013]. More albite-rich feldspar coexists with high-silica melts as in dacite, whereas andesite-calcite reaction produced more anorthite-rich feldspars (Figure 5). This is exemplified in Italian, Grecian, North American, and Canadian skarns [*Grammatikopoulos et al.*, 2005; *Piochi et al.*, 2006; *Spandler et al.*, 2012], where elevated anorthite proportion coincides with silica undersaturation. In some instances, feldspar is concentrated in garnet-poor areas [*Einaudi and Burt*, 1982b; *Baker and Lang*, 2003; *Aleksandrov*, 2011; *Groppo et al.*, 2013] and in endoskarns [*Kerrick*, 1977], proximal to the intrusion, as seen in experiments.

Since scapolite is a replacement in the reaction:

$$An + Cc \rightarrow Sc \tag{6}$$

scapolite grains form along the interaction front where carbonate and feldspar can interact. As also discussed in *Carter and Dasgupta* [2015], the increased proportion of meionite in this study's scapolites as compared to skarns, and its increased stability, may be a function of the closed-system experiments at high pressure where the fluid is water-poor and has elevated carbon dioxide activity (X_{CO2}). Andesite-calcite experiments contain meionitic scapolite at proportionately high temperatures (1100–1150°C at 0.5 GPa; Table 2) than basalt-calcite given the shift in liquidus (lower than basalt by $\leq$25°C) [*Carter and Dasgupta*, 2015]. This may suggest scapolite can form in two ways with differing stability fields: (1) as an igneous scapolite that forms at high temperatures ($\geq$1100°C) and high carbonate assimilation as with basalt-calcite and andesite-calcite reactions; and (2) as a metamorphic scapolite that is stable at conditions at which

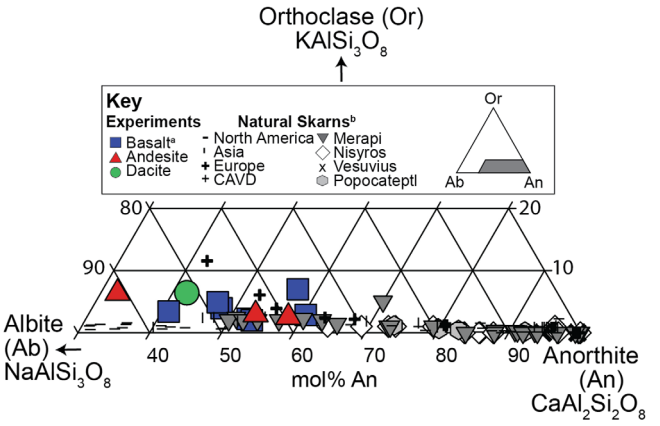

Figure 5. Feldspars are plotted on a Orthoclase (Or)-Albite (Ab)-Anorthite (An) ternary diagram, zoomed into the anorthite apex (shown as grey-shaded region on ternary in the Key) from calcite-melt reaction experiments in this study (symbols as in Figure 2: andesite, red triangles; and dacite, green circle) and *Carter and Dasgupta* [2015] (basalt[a], blue squares) as well as from several from natural skarns[b]. The location of these feldspars include: North America [*Dyer et al*., 2011; *Rasmussen et al*., 2011]; Asia [*Wenzel*, 2002; *Groppo et al*., 2013]; Eastern Europe [*Pertoldová et al*., 2009]; and several volcanic centers of interest: Colli Albani Volcanic District (CAVD) [*Federico and Peccerillo*, 2002; *Gaeta et al*., 2006; *Gozzi et al*., 2014]; Merapi, Indonesia [*Chadwick et al*., 2007, 2013]; Nisyros, Greece [*Spandler et al*., 2012]; Vesuvius, Italy [*Fulignati et al*., 2000]; and Popocatepetl, Mexico [*Sosa-Ceballos et al*., 2014].

skarnification occurs [e.g., *Shaw*, 1960; *Ellis*, 1978; *Aitken*, 1983; *Moecher and Essene*, 1990; *Moecher et al*., 1994; *Kuhn*, 2005].

Wollastonite is a run product at higher temperatures in andesite-calcite reactions and in all dacite-calcite reactions at the expense of clinopyroxene, calcite, and melt (equations (2–5), Table 2, and Figure 4d). Wollastonite has been identified in calc-silicate xenoliths erupted from actively assimilating volcanoes including Merapi [*Deegan et al*., 2010; *Troll et al*., 2013] and is common in exoskarns [e.g., *Kerrick*, 1977; *Baker and Black*, 1980; *Meinert*, 1987, 1992; *Newberry et al*., 1991; *Harley and Buick*, 1992; *Ray and Webster*, 1997; *Meinert et al*., 2005; *Marincea et al*., 2013]. Thus, as expected, it occurs as a thin layer at the calcite-silicate interface of our vertically-layered two-component capsules (Figure 1). Modal abundance of this mineral is higher at 0.5 GPa in equilibrium with the dacite starting melt as compared to andesite, because its stability declines with more mafic (e.g., high Mg, Fe content) intrusions [*Ray and Webster*, 1997].

Clinopyroxene produced in melt-calcite interaction plots consistently near the $CaMgSi_2O_6$ end-member (Figures 4d and 4e), though at low-temperature is slightly more hedenbergitic (Table 4). Clinopyroxene is abundant in endoskarns—sometimes classified as pyroxenites [e.g., *Del Moro et al*., 2001; *Rosen et al*., 2005; *Jolis et al*., 2015]—and largely plot above 50 wt.% wollastonite along the diopside-hedenbergite join as a function of the Fe/Mg ratio in the intrusion (Figure 4e and references therein) [e.g., *Harris*, 1982; *Harris and Einaudi*, 1982; *Gaeta et al*., 2006; *Piochi et al*., 2006; *Groppo et al*., 2013; *Mollo and Vona*, 2014]. With the high Fe/Mg ratio in our starting dacite mix (Table 1), the resulting clinopyroxenes are closer to a 3:4 Di-Hd ratio than those formed in andesite-calcite runs. Chemical analysis of skarn clinopyroxenes often identifies a strong Tschermak (Ca-Tschermak, CaTs, in particular, with high CaO and Al_2O_3 contents) component as well [e.g., *Morgan*, 1975; *Baker and Black*, 1980; *Bowman and Essene*, 1984; *Freda et al*., 1997, 2011; *Wenzel*, 2002; *Federico and Peccerillo*, 2002; *Gaeta et al*., 2009; *Peccerillo et al*., 2010; *Di Rocco et al*., 2012; *Spandler et al*., 2012]. This has also been noted in experiments with high calcite assimilation particularly with basalt [*Carter and Dasgupta*, 2015] and in this study with andesite (Table 4, Figures 4a and 4c).

The largest deviation between natural skarn examples and experimental mineralogy is the second of the two most dominant minerals: garnet, which is abundant in the first and absent in any of the latter [*Freda et al*., 2008; *Iacono-Marziano et al*., 2008; *Conte et al*., 2009; *Deegan et al*., 2010; *Mollo et al*., 2010a; *Jolis et al*., 2013; *Carter and Dasgupta*, 2015]. Andradite to grossular in composition, garnets are prevalent in endoskarns [*Jamtveit et al*., 1993, 1995; *Bailey*, 1997; *Pollington and Baxter*, 2010; *Lackey et al*., 2012; *Baxter and Caddick*, 2013]. A key factor in garnet stability in skarns is the carbon dioxide activity in the system wherein at high X_{CO2} diopside replaces garnet at a particular temperature [e.g., see *Meinert et al*., 2005, Figure 4]. The presence of residual calcite indicates experiments are calcite-saturated and therefore have high CO_2 activity much like carbonate-contaminated Italian CAVD lavas which contain primary calcite and are also devoid of garnet. Yet, ejecta from Vesuvius contains both garnet and calcite [*Pascal et al*., 2009] and many skarns do not consume their carbonate host rock in entirety while crystallizing garnet [e.g., *Kerrick*, 1977; *Harris and Einaudi*, 1982; *Newberry*, 1982; *Meinert et al*., 2005; *Dziggel et al*., 2009]. It may instead be that nature is usually an open system keeping carbon dioxide activity relatively low (e.g., $X_{CO2} \leq 0.4$) [*Aitken*, 1983; *Brown and Essene*, 1985; *Moecher and Essene*, 1990; *Pan et al*., 1994; *Bowman*, 1998; *Meinert et al*., 2005]. In a laboratory

environment, experiments represent a closed system, preventing any CO_2 from releasing during calcite decarbonation and keeping X_{CO2} heightened, as qualitatively confirmed by the presence of meionite scapolite. Another possible explanation to increase X_{CO2} is the higher experimental pressure over most natural skarn examples (e.g., $\leq$0.1 GPa) [*Einaudi et al*., 1981; *Einaudi and Burt*, 1982a; *Harris*, 1982; *Aitken*, 1983; *Harley and Buick*, 1992; *Pan et al*., 1994; *Bowman*, 1998; *Wenzel*, 2002; *Baker and Lang*, 2003; *Pascal et al*., 2009; *Gozzi et al*., 2014; *Marincea et al*., 2013], which permits higher water solubility in the melt [*Dixon et al*., 1995; *Papale*, 1999; *Papale et al*., 2006] partitioning a higher proportion of carbon dioxide into the fluid, preferentially stabilizing pyroxene over garnet.

4.3. Assimilation to Skarnification Transition

Assimilation is the magmatic endmember to magma-carbonate interaction, whereas metasomatic skarnification is a cooler, potentially shallower and more late-stage process of intrusion into carbonate substrates. From the above discussion, it is clear that with decreasing temperature and increasing silica content of the intruding magma, the experimental results more closely resemble skarn-like mineralogy. Similarly, the associated melt composition (dacite to rhyolite; Figure 2) more nearly matches the granitic to monzonitic compositions found by skarns, with negligible magma composition contamination [e.g., *Einaudi et al*., 1981; *Einaudi and Burt*, 1982a,1982b; *Meinert*, 1992]. This suggests that silicic ($SiO_2 > 60$ wt.%) intruding melts with a respectively lower liquidus temperature (i.e., $<$1100°C) assimilate less calcite, alternatively metasomatizing calcite to a notably skarn-like mineralogy along the magma-carbonate interface. In contrast, assimilation is the more likely process in higher temperature, more mafic systems. With high temperatures (i.e., $>$1100°C) and mafic compositions ($SiO_2 <$60 wt.%) assimilation can be extreme (up to $\sim$65%; Figure 3), similar to high estimates in Norway and at Vesuvius ($\leq$60% assimilation) [*Del Moro et al*., 2001; *Barnes et al*., 2005], and during the 2006 Merapi eruption ($\leq$80% of released CO_2 crustally-sourced) [*Troll et al*., 2012].

This conclusion proposes a hypothetical evolution-dependent sequence of magma-carbonate interaction, assuming certain conditions (Figure 6, discussed below). A more primary, initially supraliquidus intruded magma may assimilate a significant proportion ($\geq$20%) of the immediate surrounding carbonate at depth, while still hot, even more so with andesite than basalt (Figure 3b). Assimilation with mafic and intermediate magmas is exemplified in several present-day volcanic systems, such as Mounts Etna, Vesuvius, and Merapi (see Introduction) through the evidence of crustal isotopic signatures, calc-silicate xenoliths, high CO_2 degassing rates, and ultracalcic melt inclusions that may also suggest the existence of these calcite-consumed melts in dormant or extinct subarc systems [e.g., *Chadwick et al*., 2007; *Deegan et al*., 2010; *Dallai et al*., 2011; *Spandler et al*., 2012; *Troll et al*., 2013; *Carter and Dasgupta*, 2015; *Jolis et al*., 2015b]. A shallower, more evolved magma can assimilate less, particularly if it has cooled and has a lower available melt mass due to crystallization. In addition, progressively shallowing magma chambers experience proportionately decreasing water solubility with pressure, forcing water-rich arc magmas to exsolve an aqueous fluid phase, even more so if the melt intakes any CO_2 or drops below its liquidus [e.g., *Papale*, 1999; *Liu et al*., 2005; *Papale et al*., 2006]. Thus, in stratigraphically separated sills or chambers spanning various crustal depths [e.g., *Annen et al*., 2005], decarbonation may occur to a high degree due to assimilation in intermediate and mafic magmas at depth and, either later (on the order of $10^{4–6}$ years) [e.g., *Annen et al*., 2005; *Paterson et al*., 2011] or concurrently, decarbonation may occur to a lesser degree in more evolved magma compositions nearer the surface largely via hydrothermal processes as exemplified by melt inclusion compositions and volatile contents from Mount Merapi [*Nadeau et al*., 2013a].

4.4. Limits to Decarbonation

The possibility of a single system following the above trend of assimilation to skarnification through to completion during its lifespan requires first that the conditions for these reactions are met, and second that there are no limiting factors.

As noted above, for assimilation to occur, there first needs to be melt available to consume calcite. Assuming the melt composition can dissolve calcite, assimilation therefore depends on melt fraction (Figure 3b). Inherently, this implies that lower pressures and higher temperatures are correlated with higher assimilation percentages.

The composition of melt must additionally be considered as evidenced by this study, likely as a function of calcite solubility. Contaminated by consumed calcite, melt composition changes with assimilation percent

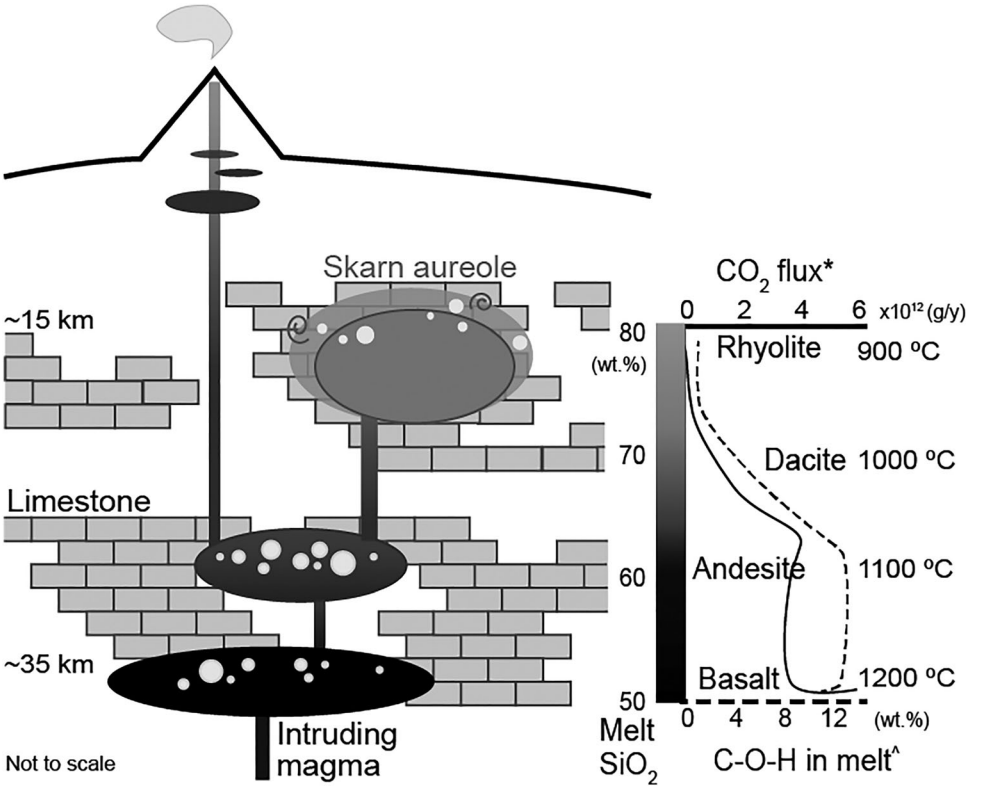

Figure 6. Schematic shows crustal limestone assimilation from lower to midcrustal pressures by subarc intrusive magmas with a graph depicting CO_2 flux* and C-O-H volatiles dissolved in the melt (estimated from EMPA deficit; Table 3) changing as the melt evolves (increasing wt.% SiO_2 with decreasing pressure). At depth (~35 km) an intruding magma is basaltic and hot (~1200°C, see color scale), and assimilates up to 20%a. Allowing remaining uncontaminated and uncrystallized melt to evolve and ascend, at 0.8 GPa, 1125°C andesite can assimilate 61% calcite and though the melt available is smaller, causing the flux of CO_2 to remain fairly steady. At 15 km, the residual melt, a cooler (1000°C) dacitic composition produces significantly less CO_2 from 13% assimilation. If the last proportion of melt cools further (900°C) and crystallizes, the residual rhyolitic melt can only assimilate ~1% of calcite. However, fluids exsolved from the pluton due to decreasing solubility (see graph) can release further carbon dioxide from skarnification. This stepwise evolutionary and ascending system (from basalt at 35 km and 1200°C to a smaller mass of rhyolite melt at 15 km and 900°C) with continuous and unlimited reaction with carbonate can contribute as much as 3.7×10^{14} g/y CO_2 (see text for further discussion).

to higher CaO, which dilutes the polymerizing oxides SiO_2 and Al_2O_3 (Table 3). In more detail, low pressure mafic melts have the highest CaO/SiO_2 ratio (Figure 3a), which in turn is evidenced by ultracalcic ($CaO/Al_2O_3 > 1$, $CaO > 13$ wt.%) melts. Likely complexing with CO_3^{2-} in the melt, Ca^{2+} is most augmented in higher pressure (1.0 and 0.8 GPa) and more mafic (andesite and basalt) starting melts [*Carter and Dasgupta*, 2015]. This may be a function of lower starting melt polymerization permitting increased calcite solubility [*Fine and Stolper*, 1985, 1986; *Stolper and Holloway*, 1988; *Blank and Brooker*, 1994; *Thibault and Holloway*, 1994; *Dixon et al*., 1995; *Dixon*, 1997; *Iacono-Marziano et al*., 2012; *Shishkina et al*., 2014]. Indeed, percent assimilation increases with NBO/T* (a ratio that quantifies polymerization by dividing the moles of Non-Bridging Oxygen by Tetrahedra—silicon, aluminum, ferric iron, titanium, and phosphorus—with * indicating all iron treated as tetrahedral Fe^{2+}, after *Brooker et al*. [2011]) and similarly with π^* (a ratio of the weighted sum of cations—calcium, potassium, sodium, magnesium and iron—over tetrahedra—silica and aluminna—after *Shishkina et al*. [2014]), which is fairly well inversely correlated to $SiO_2+Al_2O_3$ (wt.%) content [after *Moussallam et al*., 2014] in both the starting melt and contaminated melts (Table 3).

Melt polymerization and carbonate solubility is likely also affected by water content [e.g., *Papale*, 1999; *Duncan and Dasgupta*, 2014]. Although all starting melts used in this study are hydrous, there is some variation in the exact water content (Table 1). The andesite, which contains the most H_2O by $> \sim 1.8$ wt.% over previously investigated basalt [*Carter and Dasgupta*, 2015] and almost double the amount in our hydrous dacite, is also incidentally the melt capable of assimilating the most calcite. Unable to deconvolve the role of water from the effects of the major element composition of silicate starting materials in

this study, it is possible that lower water content in an otherwise compositionally identical intruding melt may independently lessen the extent of maximum assimilation, though further work is needed to isolate this factor.

The system as a whole can also reach CO_2 saturation if it remains closed. Decarbonation reactions (e.g., see equations (1–5)) will only proceed if more reactants than products—including CO_2—are available. Continuous or at least sporadic release of CO_2 through magma exsolution in a volcanic vent [*Ferlito et al*., 2014; *Fiege et al*., 2014a, 2014b, 2015; *Blythe et al*., 2015] or fluid percolation through cracks or porous media which may even be a result of carbonate breakdown [*Meinert et al*., 2005; *D'Errico et al*., 2012; *Antonellini et al*., 2013; *Heap et al*., 2013; *Mollo et al*., 2013] will prevent X_{CO2} from approaching unity.

As with CO_2, to avoid reaching calcite saturation, the melt must lose calcium for assimilation to continue. This can be achieved either by removal through crystallization of e.g., pyroxenite cumulates or through dilution by magmatic recharge. To confirm the first, further work is needed to determine the crystallization of an ultracalcic melt. The second is likely given that present-day carbonate-assimilating volcanoes indicate a significant amount of uncontaminated magma mixes with carbonate-assimilated magma ($\leq$60–92% at supraliquidus conditions with various magma compositions; see discussion below).

Although magmatic or aqueous interaction with carbonate is a relatively rapid process [*Jamtveit*, 1991; *Bergantz*, 2000; *Clechenko and Valley*, 2003; *Deegan et al*., 2010; *Raimondo et al*., 2012; *Jolis et al*., 2013; *Ferry*, 2016], in order to degas a maximum amount of carbon dioxide a magmatic system requires time, to remain below saturation, and the pressure-temperature-compositional conditions necessary to react with the surrounding limestone. Additionally to consider this process as a contributor of CO_2 to the atmospheric reservoir, the assumption must be made that a little is sequestered into carbonate minerals through precipitation from fluids or igneous crystallization [*White et al*., 1999, 2005; *Caciagli and Manning*, 2003; *Gozzi et al*., 2014; *Galvez et al*., 2015].

4.5. CO_2 Output

Recent work has identified significant sources of CO_2 from several previously unconsidered processes and locations including passive volcanic degassing (i.e., lava lakes), diffuse degassing in e.g., hydrothermally active areas like Italy, tectonic magmatic degassing as in the East African Rift Zone, and certainly additional release due to magma-carbonate interaction [e.g., *Chiodini et al*., 2004; *Iacono-Marziano et al*., 2008; *Troll et al*., 2012; *Burton et al*., 2013; *Lee et al*., 2016].

As expected, increased calcite consumption will release increasing amounts of carbon dioxide from a degassing magma ($\leq 2.9 \times 10^{11}$ g/y in andesite-calcite reactions versus $\leq 8.1 \times 10^{10}$ g/y max in dacite-calcite reactions, at a single volcano with magma flux of 10^{12} g/y), either from the melt as solubility decreases with pressure [*Wallace et al*., 1995; *Papale*, 1999; *Wallace*, 2005; *Papale et al*., 2006; *Blythe et al*., 2015; *Duncan and Dasgupta*, 2015] or from the release of a separate CO_2-rich fluid phase as mentioned above. Compiling experimental assimilation estimates from this study and *Carter and Dasgupta* [2015] can provide a simple example of an expected ascent and cooling path for an intruded magma body as it evolves from basalt to andesite to dacite, based on the timescales mentioned above and ignoring possible limitations discussed in the previous section. As is shown in Figure 6, if the initial injection at $\sim$35 km is supraliquidus ($\sim$1200°C) basalt, assimilation is $\sim$20%, thus it could produce as much as $\sim 5.6 \times 10^{12}$ g/y CO_2 given that 44 wt.% of calcite is CO_2 for a pluton magma flux somewhere between background and surge estimates (10^{14} g/y; using volume flux based on exposed batholith dimensions from *Paterson et al*. [2011] and thermal constraints from *Menand et al*. [2015], as well as density calculations for each composition after *Bottinga and Weill* [1970]). After some heat loss to assimilation and the surrounding crust, the melt evolves and crystallizes ($F\sim$70%), and the assimilation drops. Assuming also that only half of the melt became calcite-contaminated in the last step, leaving 50 wt.% of the remaining melt to react with calcite, this frees 3.5×10^{12} g/y of sequestered CO_2. Let's assume again half of the remaining uncontaminated melt ($F\sim$30% of the original basalt, based on matching silica content between calcite-free andesite melts in Table 3 and those of basalt in *Carter and Dasgupta* [2015]), now a basaltic andesite and 1150°C, ascends further into the crust to $\sim$0.8 GPa. Interaction with calcite here would release a similar amount ($\sim 3.5 \times 10^{12}$ g/y CO_2). At a lower temperature and becoming andesitic in composition the remaining melt, which can assimilate the most (>60%), but has a smaller melt mass (half of $F\sim$24%), ultimately releases slightly more carbon ($\sim 3.9 \times 10^{12}$ g/y CO_2). This is followed again by less decarbonation with further cooling (1100°C, $F\sim$18%,

$\sim$1.7 $\times$ 10^{12} g/y CO_2). Either the magma can rise rapidly to the surface (or near-surface reservoirs) where it can be ejected in a volcanic eruption, or it can rise to shallower levels (i.e., $\sim$15 km) and pond in the crust. Stalling here, the melt differentiates into dacite ($F\sim$15%) and falls below 1100°C. At this stage, assimilation plummets in the remaining melt and thus only $\sim$3.1 $\times$ 10^{11} g/y CO_2 escapes. The pluton continues to cool to 900°C at which point crystallization leaves the residual melt ($F<$1%) granitic in composition, which experiences almost no assimilation, but exsolves water since low pressure and high polymerization lower solubility. The fluid can percolate into the remaining surrounding carbonate where metasomatism produces a skarn aureole that can penetrate deeper into the wall rock perhaps releasing further CO_2 due to mineralogical reactions that replace calcite with calc-silicates [*Einaudi and Burt*, 1982b; *Barton and Hanson*, 1989; *Ferry and Gerdes*, 1998; *Bergantz*, 2000; *D'Errico et al*., 2012; *Lackey et al*., 2012; *Yardley and Cleverley*, 2013; *Ganino et al*., 2013; *Groppo et al*., 2013; *Nadeau et al*., 2013b; *Capasso et al*., 2014].

In total, ignoring potential skarnification and any carbon originating from the basalt's mantle source, this demonstrative evolving magmatic system can release on the order of $\sim$1.9 $\times$ 10^{12} to $<\sim$3.7 $\times$ 10^{14} g of CO_2 into the atmosphere for a typical pluton flux range ($10^{13}-10^{15}$ g/y)—or up to five orders of magnitude higher with magma fluxing via conduit or diaper injection [*Paterson et al*., 2011]—from primitive liquid intrusion at depth to complete crystallization in the midcrust, in a duration of $10^{3}-10^{4}$ years [*Annen et al*., 2005; *Paterson et al*., 2011]. This estimate depends on the rate of crystallization in the last pluton-forming step, which may be expedited by the calcite-assimilated raised liquidus discussed earlier, the proportion of uncontaminated magma, and also assumes no assimilation limitations besides *P-T-X* conditions (e.g., continuous limestone-magma interaction, no major CO_2 sequestration in e.g., veins or scapolite). With that lifespan, the time-averaged flux is $\leq$1.9 $\times$ 10^{11} g/y CO_2. However, it is far more likely that a magmatic system will recharge than exist only as a single evolving and ascending pulse of basalt, instead experiencing assimilation simultaneously in basaltic and andesitic sills at depth and in shallow, silicic magma chambers. In this case, that total mass of CO_2 may be released over a much shorter time frame, such that the average flux in a single system may increase by an order of magnitude.

If a large number of magmatic systems (e.g., 87–130 volcanoes globally) [see *Carter and Dasgupta*, 2015] are undergoing assimilation within one time period, e.g., the Cretaceous [*Lee et al*., 2013], then the magma composition can make a massive difference in the amount of excess CO_2, in addition to any that the mantle- or subduction-modified, mantle-derived magma already carried, being degassed from crustal sources. A more primary composition, fully molten, can release (allowing all melt to interact with calcite, though results are still significant if 50 wt.% contaminated melt is again used) $\sim$10–20 times (3.7–5.6 $\times$ 10^{15} g/y) [*Carter and Dasgupta*, 2015] as much total CO_2 as a recent high estimate of the current global arc volcanic flux from *Burton et al*. [2013], whereas andesite magma, a more common continental arc composition [*Kelemen et al*., 2014], at a lower melt fraction (e.g., 70%) expels $\sim$20–25 times (4.8–7.1 $\times$ 10^{15} g/y) and dacite, (which requires at least 50% crystallization to evolve from a basalt) [e.g., *Annen et al*., 2005] $\sim$5 times (1.1–1.6 $\times$ 10^{15} g/y). Our calculations may in fact yield as much as $\sim$20–85 times the current global arc volcanic flux with molten basalt, $\sim$30–110 time with partially crystallized andesite, and $\sim$5–25 times with partially crystallized dacite if compared against other relatively lower estimates of present-day arc CO_2 outflux from *Dasgupta and Hirschmann* [2010] and *Kelemen and Manning* [2015]. Other estimates of present-day global arc CO_2 flux that are used in literature [*Sano and Williams*, 1996; *Dasgupta*, 2013] are even lower, which can extend these values to $\sim$130 times the current global arc CO_2 flux estimate with basalt, $\sim$165 times with andesite, and $\sim$35 times with dacite. Although the relative importance of continental crust-derived CO_2 varies depending both on the present-day global outflux of CO_2 from island-arc dominated subduction zones and the number of carbonate assimilating volcanoes in the past, it is clear that the contribution from assimilation can drastically change the total volcanic CO_2 output in the Cretaceous.

At present, evidence suggests at least four volcanoes in particular are releasing crustal in addition to mantle-derived CO_2 (Vesuvius, Etna, Merapi, and Popocatepetl; see Introduction). Assuming typical arc magmas contain about 3000 ppm CO_2 [*Wallace*, 2005] with minor shifts for solubility (e.g., 2800 ppm for the hydrous dacitic composition as calculated using the model by *Papale* [1999]), then in order to match their measured CO_2 degassing rates [*Frondini et al*., 2004; *Burton et al*., 2013; *Caliro et al*., 2014], we can calculate how much additional CO_2 needs to be added from carbonate wall rock. We use estimated magma recharge rates [*Siswowidjoyo et al*., 1995; *Iacono-Marziano et al*., 2009; *Roberge et al*., 2009; *Harris et al*., 2011] and consider the particular magma composition of each system (basaltic for Etna and Vesuvius, basaltic-andesite to

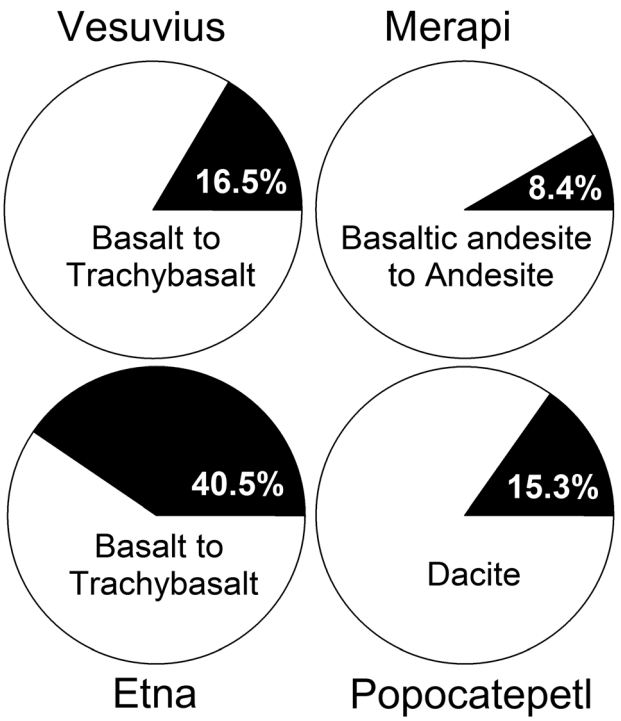

Figure 7. Pie charts depict a calculated minimum (see Discussion) proportion (in percent, as labeled) of a magma chamber that must be calcite-contaminated melt for four presently active carbonate-assimilating active volcanoes based on their measured CO_2 output [*Burton et al.*, 2013]. Calculations use similar compositions to those suggested in the literature (basaltic for Etna and Vesuvius, basaltic-andesite to andesitic at Merapi, and evolved dacite-like compositions at Popocatepetl; *Gertisser and Keller*, 2003; *Troll et al.*, 2013; *Correale et al.*, 2014; *Pichavant et al.*, 2014; *Sosa-Ceballos et al.*, 2014], and assume the chamber is at ~15 km depth and the melt is above its specific (calcite-free) liquidus (1200, 1175, 1100°C for basalt, andesite, and dacite, respectively), and that uncontaminated melt (white) contains typical arc CO_2 contents around 3000 ppm [*Papale*, 1999; *Wallace*, 2005].

andesitic at Merapi, and evolved dacite-like compositions at Popocatepetl) [*Gertisser and Keller*, 2003; *Troll et al.*, 2013; *Correale et al.*, 2014; *Pichavant et al.*, 2014; *Sosa-Ceballos et al.*, 2014]. Given the assimilation percentages determined in this study for intermediate and silicic melt compositions (Figure 3b), estimates call for a significant though varying proportion of the magma chamber to be contaminated by assimilated calcite. A partially molten magma chamber (F~30%) would require more assimilation to meet CO_2 demands, whereas only a portion of a superliquidus chamber would need to interact with calcite. In this range, Popocatepetl would need ~nearly all to 15% contaminated melt, Merapi ~99–8%, and for the Italian volcanoes, Vesuvius requires ~38–17%, whereas Etna calls for as much as ~92–40% contaminated melt (Figure 7). These represent maximum estimates due to the probability that carbonate assimilation is not a continuous or homogeneous process, as discussed above, and unlike near-equilibrium experiments, may be a limited reaction. Additionally, these calculations assume no change in recharge rate, which can increase during eruptions.

5. Concluding Remarks

Presently active mafic volcanoes, such as at Mounts Etna and Vesuvius, provide evidence that crustal decarbonation by assimilation may be a source of excess CO_2 degassing in addition to the typical mantle-sourced carbon to the atmosphere. Extinct magmatic systems now identified by exposed plutons, such as in the Sierra Nevadas, indicate prior decarbonation by skarnification. Previous experimental investigations constrain CO_2 release by assimilation [e.g., *Iacono-Marziano et al.*, 2007, 2009; *Deegan et al.*, 2010; *Troll et al.*, 2012; *Carter and Dasgupta*, 2015], and some calculations indicate skarnification may also release significant amounts of the gas from the crust [*Lee et al.*, 2013; *Lee and Lackey*, 2015]. There may be limiting factors such as skarn barrier [*Gaeta et al.*, 2009], thermal barrier [*Watkinson and Wyllie*, 1969; *Kerrick*, 1977], and calcite saturation point [*Carter and Dasgupta*, 2015]. The first two require "death" of the magma chamber in terms of a lack of convection and/or heat loss. The latter, wherein the melt becomes silica-undersaturated and ultracalcic [This Study; *Watkinson and Wyllie*, 1964; *Carter and Dasgupta*, 2015] suggests magma chamber volume and recharge has some control. This will ultimately dictate extent of decarbonation.

Therefore, the melt fraction (F)—and thus the pressure (P), temperature (T), and composition (X)—of the system must be high enough for active calcite consumption. Dropping temperature alone in an e.g., andesite-calcite system (lowering F^* from >80 to ~32%) subsequently stifles assimilation (65 to <2%). Similarly, allowing a supraliquidus melt of high silica-content to interact with a pure calcite also diminishes assimilation (>60% with andesite to <20% dacite) thereby indicating a compositional control on calcite saturation level in the melt. In conjunction with less calcite consumption, we find that the skarn mineral wollastonite becomes more abundant in magmas less primitive than basalt.

We determine two orders of magnitude greater CO_2 release given a standard and constant magma flux and unlimited limestone interaction with hydrous andesitic over hydrous dacitic compositions. Hotter, intermediate melts can release $\leq 2.9 \times 10^{11}$ g of CO_2/y at a single typical arc volcano, whereas cooler, though still supraliquidus, dacites on the other hand will expel an excess of only $\leq 8.1 \times 10^{10}$ g of CO_2/y at a typical arc volcano magma recharge rate. In support, diffuse CO_2 has been found to produce only ~50% the amount of CO_2 degassed at the edifice of Vesuvius [*Frondini et al*., 2004; *Burton et al*., 2013]. Total CO_2 released at different volcanoes depends on the relative proportions of the magma in the system undergoing carbonate assimilation, which is melt composition-controlled (e.g., ≥17% at [trachy]basaltic Vesuvius versus ≥15% at dacitic Popocatepetl, back-calculated based on gas emission).

An ascending and evolving magma may over a potential lifetime of 1 Myr recycle a substantial amount (≤~0.4 Gt) of CO_2—or more, if recharge permits simultaneous and repeated assimilation at several depths within a system in limestone crust, or plumbing geometry changes—from carbonate wall rock into the atmosphere. Extrapolating to global scales in geologic history, a larger proportion of CO_2 was likely released by assimilation to the atmosphere during initial intrusion of a mafic magma into a carbonate substrate than as the magma chamber differentiated towards granite.

Though further investigation is needed to quantify any additional CO_2 released by metasomatic decarbonation by the pluton's aureole and limitations to these processes, crustal carbonate assimilation and skarnification by intruding and evolving magmatic bodies may together be a significant contribution to atmospheric CO_2 and perhaps be a control in long-term climate change.

Acknowledgments
We acknowledge helpful discussions with Michelle Gevedon and Jaime Barnes at UT Austin, and Jade Star Lackey at Pomona College regarding skarnification. We also thank Frances Deegan and Calvin Barnes for their critical reviews and insightful suggestions toward the clarity of the manuscript. Supporting data are included as supporting information Table S1 in an SI file; any additional data may be obtained from L.B.C. (email: lbc2@rice.edu). This research was funded by U.S. NSF grant OCE 1338842 and a Sloan Foundation (Deep Carbon Observatory) officer grant.

References

Afanasyev, A., A. Costa, and G. Chiodini (2015), Investigation of hydrothermal activity at Campi Flegrei caldera using 3D numerical simulations: Extension to high temperature processes, *J. Volcanol. Geotherm. Res.*, *299*, 68–77.
Aitken, B. G. (1983), T-X_{CO2} stability relations and phase equilibria of a calcic carbonate scapolite, *Geochem. Cosmochim. Acta*, *47*, 351–362.
Aleksandrov, S. M. (2011), Metasomatic transformations of carbonate rocks observable in quarries of Riverside, California, United States, *Geochem. Int.*, *49*(7), 711–725.
Annen, C., J. D. Blundy, and S. J. Sparks (2005), The genesis of intermediate and silicic magmas in deep crustal hot zones, *J. Petrol.*, *47*(3), 505–539.
Antonellini, M., A. Cilona, E. Tondi, M. Zambrano, and F. Agosta (2013), Fluid flow numerical experiments of faulted porous carbonates, Northwest Sicily (Italy), *Mar. Pet. Geol.*, *55*, 186–201.
Bailey, D. (1997), Heat Capacity of Minerals: A hands-on introduction to chemical thermodynamics, in *Teaching Mineralogy*, edited by J. B. Brady, D. W. Mogk, and D. Perkins, III, pp. 131–142, Mineralogical Society of America, Washington, D.C.
Baker, C. K., and P. M. Black (1980), Assimilation and metamorphism at a basalt-limestone contact, Tokatoka, New Zealand, *Mineral. Mag.*, *43*(330), 797–807.
Baker, T., and J. R. Lang (2003), Reconciling fluid inclusion types, fluid processes, and fluid sources in skarns: An example from the Bismark deposit, Mexico, *Miner. Deposita*, *38*(4), 474–495.
Barberi, F., and L. Leoni (1980), Metamorphic carbonate ejecta from vesuvius plinian eruptions: Evidence of the occurrence of shallow magma chambers, *Bull. Volcanol.*, *43*(1), 107–120.
Barnes, C. G., T. Prestvik, B. Sundvoll, and D. Surratt (2005), Pervasive assimilation of carbonate and silicate rocks in the Hortavaer igneous complex, north-central Norway, *Lithos*, *80*, 179–199.
Barton, M. D., and R. B. Hanson (1989), Magmatism and the development of low-pressure metamorphic belts: Implications from the western United States and thermal modeling, *Geol. Soc. Am. Bull.*, *101*, 1051–1065.
Baxter, E. F., and M. J. Caddick (2013), Garnet growth as a proxy for progressive subduction zone dehydration, *Geology*, *41*(6), 643–646.
Bergantz, G. W. (2000), Metamorphism and anatexis in the mafic complex contact aureole, Ivrea Zone, Northern Italy, *J. Petrol.*, *41*(8), 1307–1327.
Blank, J. G., and R. A. Brooker (1994), Experimental studies of carbon dioxide in silicate melts; solubility, speciation, and stable carbon isotope behavior, *Rev. Mineral. Geochem.*, *30*(1), 157–186.
Blythe, L. S., F. M. Deegan, C. Freda, E. M. Jolis, M. Masotta, V. Misiti, J. Taddeucci, and V. R. Troll (2015), CO_2 bubble generation and migration during magma–carbonate interaction, *Contrib. Mineral. Petrol.*, *169*(4), 1–16, doi:10.1007/s00410-015-1137-4.
Bottinga, Y., and D. F. Weill (1970), Densities of liquid silicate systems calculated from partial molar volumes of oxide components, *Am. J. Sci.*, *269*, 169–182.
Bowman, J. R. (1998), Basic Aspects and applications of phase equilibria in the analysis of metasomatic Ca-Mg-Al-Fe-Si skarns, *Mineral. Assoc. Can. Short Course Ser.*, *26*, 1–49.
Bowman, J. R., and E. J. Essene (1984), Contact skarn formation at Elkhorn, Montana. I: P-T-Component activity conditions of early skarn formation, *Am. J. Sci.*, *284*, 597–650.
Brooker, R. A., R. S. J. Sparks, J. L. Kavanagh, and M. Field (2011), The volatile content of hypabyssal kimberlite magmas: Some constraints from experiments on natural rock compositions, *Bull. Volcanol.*, *73*(8), 959–981.
Brown, P. E., and E. J. Essene (1985), Activity variations attending tungsten skarn formation, Pine Creek, California, *Contrib. Mineral. Petrol.*, *89*(4), 358–369.
Brown, P. E., J. R. Bowman, and W. C. Kelly (1985), Petrologic and stable isotope constraints on the source and evolution of skarn-forming fluids at Pine Creek, California, *Econ. Geol.*, *80*, 72–95.
Burton, M. R., G. M. Sawyer, and D. Granieri (2013), Deep carbon emissions from volcanoes, *Rev. Mineral. Geochem.*, *75*, 323–354.

Caciagli, N. C., and C. E. Manning (2003), The solubility of calcite in water at 6-16kbar and 500-800°C, *Contrib. Mineral. Petrol.*, *146*(3), 275–285.
Caliro, S., G. Chiodini, R. Avino, C. Cardellini, and F. Frondini (2005), Volcanic degassing at Somma–Vesuvio (Italy) inferred by chemical and isotopic signatures of groundwater, *Appl. Geochem.*, *20*(6), 1060–1076.
Caliro, S., G. Chiodini, and A. Paonita (2014), Geochemical evidences of magma dynamics at Campi Flegrei (Italy), *Geochim. Cosmochim. Acta*, *132*, 1–15, doi:10.1016/j.gca.2014.01.021.
Capasso, G., C. Federico, P. Madonia, and A. Paonita (2014), Response of the shallow aquifer of the volcano-hydrothermal system during the recent crises at Vulcano Island (Aeolian Archipelago, Italy), *J. Volcanol. Geotherm. Res.*, *273*, 70–80.
Carter, L. B., and R. Dasgupta (2015), Hydrous basalt–limestone interaction at crustal conditions: Implications for generation of ultracalcic melts and outflux of CO_2 at volcanic arcs, *Earth Planet. Sci. Lett.*, *427*, 202–214.
Chadwick, J. P., V. R. Troll, D. Morgan, R. Gertisser, T. E. Waight, J. P. Davidson, and C. Ginibre (2007), Carbonate Assimilation at Merapi Volcano, Java, Indonesia: Insights from Crystal Isotope Stratigraphy, *J. Petrol.*, *48*(9), 1793–1812.
Chadwick, J. P., V. R. Troll, T. E. Waight, F. M. Zwan, and L. M. Schwarzkopf (2013), Petrology and geochemistry of igneous inclusions in recent Merapi deposits: A window into the sub-volcanic plumbing system, *Contrib. Mineral. Petrol.*, *165*(2), 259–282.
Chiodini, G., and F. Frondini (2001), Carbon dioxide degassing from the Albani Hills volcanic region, Central Italy, *Chem. Geol.*, *177*, 67–83.
Chiodini, G., F. Frondini, and F. Ponziani (1995), Deep structures and carbon dioxide, *Geothermics*, *24*(1), 81–94.
Chiodini, G., C. Cardellini, A. Amato, E. Boschi, S. Caliro, F. Frondini, and G. Ventura (2004), Carbon dioxide Earth degassing and seismogenesis in central and southern Italy, *Geophys. Res. Lett.*, *31*, L07615, doi:10.1029/2004GL019480.
Chiodini, G., S. Caliro, A. Aiuppa, R. Avino, D. Granieri, R. Moretti, and F. Parello (2010), First $^{13}C/^{12}C$ isotopic characterisation of volcanic plume CO_2, *Bull. Volcanol.*, *73*(5), 531–542.
Clechenko, C. C., and J. W. Valley (2003), Oscillatory zoning in garnet from the Willsboro Wollastonite Skarn, Adirondack Mts, New York: A record of shallow hydrothermal processes preserved in a granulite facies terrane, *J. Metamorph. Geol.*, *21*(8), 771–784.
Conte, A. M., D. Dolfi, M. Gaeta, V. Misiti, S. Mollo, and C. Perinelli (2009), Experimental constraints on evolution of leucite-basanite magma at 1 and 10^{-4} GPa: Implications for parental compositions of Roman high-potassium magmas, *Eur. J. Mineral.*, *21*(4), 763–782.
Correale, A., A. Paonita, M. Martelli, A. Rizzo, S. G. Rotolo, R. A. Corsaro, and V. Di Renzo (2014), A two-component mantle source feeding Mt. Etna magmatism: Insights from the geochemistry of primitive magmas, *Lithos*, *184-187*, 243–258.
D'Errico, M. E., J. S. Lackey, B. E. Surpless, S. L. Loewy, J. L. Wooden, J. D. Barnes, A. Strickland, and J. W. Valley (2012), A detailed record of shallow hydrothermal fluid flow in the sierra nevada magmatic arc from low-$\delta^{18}O$ skarn garnets, *Geology*, *40*(8), 763–766.
Dallai, L., R. Cioni, C. Boschi, and C. D'Oriano (2011), Carbonate-derived CO_2 purging magma at depth: Influence on the eruptive activity of Somma-Vesuvius, Italy, *Earth Planet. Sci. Lett.*, *310*(1-2), 84–95.
Dasgupta, R. (2013), Ingassing, Storage, and Outgassing of Terrestrial Carbon through Geologic Time, *Rev. Mineral. Geochem.*, *75*, 183–229.
Dasgupta, R., and M. M. Hirschmann (2010), The deep carbon cycle and melting in Earth's interior, *Earth Planet. Sci. Lett.*, *298*(1-2), 1–13.
Dasgupta, R., A. Mallik, K. Tsuno, A. C. Withers, G. Hirth, and M. M. Hirschmann (2013), Carbon-dioxide-rich silicate melt in the Earth's upper mantle., *Nature*, *493*, 211–215.
Deegan, F. M., V. R. Troll, C. Freda, V. Misiti, J. P. Chadwick, C. L. McLeod, and J. P. Davidson (2010), Magma-carbonate interaction processes and associated CO_2 release at Merapi Volcano, Indonesia: Insights from experimental petrology, *J. Petrol.*, *51*(5), 1027–1051.
Deegan, F. M., V. R. Troll, C. Freda, V. Misiti, and J. P. Chadwick (2011), Fast and furious: Crustal CO_2 release at Merapi volcano, Indonesia, *Geol. Today*, *27*, 63–64.
Del Moro, A., P. Fulignati, P. Marianelli, and A. Sbrana (2001), Magma contamination by direct wall rock interaction: Constraints from xenoliths from the walls of a carbonate-hosted magma chamber (Vesuvius 1944 eruption), *J. Volcanol. Geotherm. Res.*, *112*, 15–24.
Di Rocco, T., C. Freda, M. Gaeta, S. Mollo, and L. Dallai (2012), Magma Chambers Emplaced in Carbonate Substrate: Petrogenesis of Skarn and Cumulate Rocks and Implications for CO_2 Degassing in Volcanic Areas, *J. Petrol.*, *53*(11), 2307–2332.
Dixon, J. (1997), Degassing of alkalic basalts, *Am. Mineral.*, *82*, 368–378.
Dixon, J. E., E. M. Stolper, and J. R. Holloway (1995), An experimental study of water and carbon dioxide solubilities in mid-ocean ridge basaltic liquids. Part I: Calibration and solubility models, *J. Petrol.*, *36*(6), 1607–1631.
Duncan, M. S., and R. Dasgupta (2014), CO_2 solubility and speciation in rhyolitic sediment partial melts at 1.5–3.0GPa: Implications for carbon flux in subduction zones, *Geochim. Cosmochim. Acta*, *124*, 328–347.
Duncan, M. S., and R. Dasgupta (2015), Pressure and temperature dependence of CO_2 solubility in hydrous rhyolitic melt: Implications for carbon transfer to mantle source of volcanic arcs via partial melt of subducting crustal lithologies, *Contrib. Mineral. Petrol.*, *169*(54), 1–19.
Dyer, B., C. T. A. Lee, W. P. Leeman, and M. Tice (2011), Open-system behavior during pluton-wall-rock interaction as constrained from a study of endoskarns in the Sierra Nevada batholith, California, *J. Petrol.*, *52*(10), 1987–2008.
Dziggel, A., K. Wulff, J. Kolb, F. M. Meyer, and Y. Lahaye (2009), Significance of oscillatory and bell-shaped growth zoning in hydrothermal garnet: Evidence from the Navachab gold deposit, Namibia, *Chem. Geol.*, *262*, 278–292.
Einaudi, M., and D. Burt (1982a), A special issue devoted to skarn deposits: Introduction-terminology, classification, and composition of Skarn deposits, *Econ. Geol.*, *77*, 745–754.
Einaudi, M., and D. Burt (1982b), Introduction: Terminology, classification, and composition of skarn deposits, *Econ. Geol.*, *77*(4), 745–754.
Einaudi, M. T., L. D. Meinert, and R. J. Newberry (1981), Skarn Deposits, *Econ. Geol.*, *100*, 317–391.
Ellis, D. E. (1978), Stability and phase equilibria of chloride and carbonate bearing scapolites at 750°C and 4000 bar, *Geochim. Cosmochim. Acta*, *42*(8), 1271–1281.
Evans, M. J., L. A. Derry, and C. France-Lanord (2008), Degassing of metamorphic carbon dioxide from the Nepal Himalaya, *Geochem. Geophys. Geosyst.*, *9*, Q04021, doi:10.1029/2007GC001796.
Federico, M., and A. Peccerillo (2002), Mineral chemistry and petrogenesis of granular ejecta from the Alban Hills volcano (Central Italy), *Mineral. Petrol.*, *74*, 223–252.
Ferlito, C., M. Coltorti, G. Lanzafame, and P. P. Giacomoni (2014), The volatile flushing triggers eruptions at open conduit volcanoes: Evidence from Mount Etna volcano (Italy), *Lithos*, *184-187*, 447–455.
Ferry, J. M. (2016), Fluids in the crust during regional metamorphism: Forty years in the Waterville limestone, *Am. Mineral.*, *101*(2), 500–517.
Ferry, J. M., and M. L. Gerdes (1998), Chemically reactive fluid flow during metamorphism, *Annu. Rev. Earth Planet. Sci.*, *26*(1), 255–287.
Fiege, A., F. Holtz, and S. Cichy (2014a), Bubble formation during decompression of andesitic melts, *Am. Mineral.*, *99*, 1052–1062.
Fiege, A., H. Behrens, F. Holtz, and F. Adams (2014b), Kinetic vs. thermodynamic control of degassing of H_2O–S±Cl-bearing andesitic melts, *Geochim. Cosmochim. Acta*, *125*, 241–264.

Fiege, A., F. Vetere, G. Iezzi, A. Simon, and F. Holtz (2015), The roles of decompression rate and volatiles ($H_2O+Cl\pm CO_2\pm S$) on crystallization in (trachy-) basaltic magma, *Chem. Geol.*, *411*, 310–322.
Fine, G., and E. Stolper (1985), The speciation of carbon dioxide in sodium aluminosilicate glasses, *Contrib. Mineral. Petrol.*, *91*(2), 105–121.
Fine, G., and E. Stolper (1986), Dissolved carbon dioxide in basaltic glasses: Concentrations and speciation, *Earth Planet. Sci. Lett.*, *76*, 263–278.
Freda, C., M. Gaeta, D. M. Palladino, and R. Trigila (1997), The Villa Senni Eruption (Alban Hills, central Italy): The role of H2O and CO2 on the magma chamber evolution and on the eruptive scenario, *J. Volcanol. Geotherm. Res.*, *78*, 103–120.
Freda, C., M. Gaeta, V. Misiti, S. Mollo, D. Dolfi, and P. Scarlato (2008), Magma–carbonate interaction: An experimental study on ultrapotassic rocks from Alban Hills (Central Italy), *Lithos*, *101*, 397–415.
Freda, C., M. Gaeta, B. Giaccio, F. Marra, D. M. Palladino, P. Scarlato, and G. Sottili (2011), CO_2-driven large mafic explosive eruptions: The Pozzolane Rosse case study from the Colli Albani Volcanic District (Italy), *Bull. Volcanol.*, *73*(3), 241–256, doi:10.1007/s00445-010-0406-3.
Frondini, F., G. Chiodini, S. Caliro, C. Cardellini, D. Granieri, and G. Ventura (2004), Diffuse CO_2 degassing at Vesuvio, Italy, *Bull. Volcanol.*, *66*(7), 642–651.
Fulignati, P., P. Marianelli, R. Santacroce, and A. Sbrana (2000), The skarn shell of the 1944 Vesuvius magma chamber. Genesis and PTX conditions from melt and fluid inclusion data, *Eur. J. Mineral.*, *12*, 1025–1039.
Fulignati, P., C. Panichi, A. Sbrana, S. Caliro, A. Gioncada, and A. Del Moro (2005), Skarn formation at the walls of the 79AD magma chamber of Vesuvius (Italy): Mineralogical and isotopic constraints, *Neues Jahrb. Mineral. Abh.*, *181*(1), 53–66.
Gaeta, M., G. Fabrizio, and G. Cavarretta (2000), F-phlogopites in the Alban Hills Volcanic District (Central Italy): Indications regarding the role of volatiles in magmatic crystallisation, *J. Volcanol. Geotherm. Res.*, *99*, 179–193.
Gaeta, M., C. Freda, J. N. Christensen, L. Dallai, F. Marra, D. B. Karner, and P. Scarlato (2006), Time-dependent geochemistry of clinopyroxene from the Alban Hills (Central Italy): Clues to the source and evolution of ultrapotassic magmas, *Lithos*, *86*(3-4), 330–346.
Gaeta, M., T. Di Rocco, and C. Freda (2009), Carbonate assimilation in open magmatic systems: The role of melt-bearing Skarns and cumulate-forming processes, *J. Petrol.*, *50*(2), 361–385.
Galvez, M. E., C. E. Manning, J. A. D. Connolly, and D. Rumble (2015), The solubility of rocks in metamorphic fluids: A model for rock-dominated conditions to upper mantle pressure and temperature, *Earth Planet. Sci. Lett.*, *430*, 486–498.
Ganino, C., and N. T. Arndt (2009), Climate changes caused by degassing of sediments during the emplacement of large igneous provinces, *Geology*, *37*(4), 323–326.
Ganino, C., N. T. Arndt, C. Chauvel, A. Jean, and C. Athurion (2013), Melting of carbonate wall rocks and formation of the heterogeneous aureole of the Panzhihua intrusion, China, *Geosci. Front.*, *4*(5), 535–546.
Gertisser, R., and J. Keller (2003), Temporal variations in magma composition at Merapi Volcano (Central Java, Indonesia): Magmatic cycles during the past 2000 years of explosive activity, *J. Volcanol. Geotherm. Res.*, *123*, 1–23.
Ghiorso, M. S., and R. O. Sack (1995), Chemical mass transfer in magmatic processes IV. A revised and internally consistent thermodynamic model for the interpolation and extrapolation of liquid-solid equilibria in magmatic systems at elevated temperatures and pressures, *Contrib. Mineral. Petrol.*, *119*(2-3), 197–212.
Gilg, H., A. Lima, R. Somma, and H. Belkin (2001), Isotope geochemistry and fluid inclusion study of skarns from Vesuvius, *Mineral. Petrol.*, *73*, 145–176.
Goff, F., et al. (1998), Geochemical surveillance of magmatic volatiles at Popocatepetl Volcano, Mexico, *Geol. Soc. Am. Bull.*, *110*(6), 695–710.
Goff, F., S. P. Love, R. G. Warren, D. Counce, J. Obenholzner, C. Siebe, and S. C. Schmidt (2001), Passive infrared remote sensing evidence for large, intermittent CO_2 emissions at Popocatepetl, *Chem. Geol.*, *177*, 133–156.
Gozzi, F., M. Gaeta, C. Freda, S. Mollo, T. Di Rocco, F. Marra, L. Dallai, and A. Pack (2014), Primary magmatic calcite reveals origin from crustal carbonate, *Lithos*, *190-191*, 191–203.
Grammatikopoulos, T. A., A. H. Clark, T. H. Pearce, and D. A. Archibald (2005), Genesis of the olden wollastonite skarn, Sharbot Lake domain, Central Metasedimentary Belt, Grenville Province, southeastern Ontario, *Canada, Can. J. Earth Sci.*, *42*, 1401–1417.
Granieri, D., A. Costa, G. Macedonio, M. Bisson, and G. Chiodini (2013), Carbon dioxide in the urban area of Naples: Contribution and effects of the volcanic source, *J. Volcanol. Geotherm. Res.*, *260*, 52–61.
Groppo, C., F. Rolfo, D. Castelli, and J. a. D. Connolly (2013), Metamorphic CO_2 production from calc-silicate rocks via garnet-forming reactions in the CFAS–H2O–CO2 system, *Contrib. Mineral. Petrol.*, *166*(6), 1655–1675.
Grove, T. L., M. B. Baker, R. C. Price, S. W. Parman, L. T. Elkins-Tanton, N. Chatterjee, and O. Muntener (2005), Magnesian andesite and dacite lavas from Mt. Shasta, northern California: Products of fractional crystallization of H_2O-rich mantle melts, *Contrib. Mineral. Petrol.*, *148*(5), 542–565.
Hammer, J. E., K. V. Cashman, and B. Voight (2000), Magmatic processes revealed by textural and compositional trends in Merapi dome lavas, *J. Volcanol. Geotherm. Res.*, *100*(1-4), 165–192.
Harley, S., and I. Buick (1992), Wollastonite—Scapolite assemblages as indicators of granulite pressure-temperature-fluid histories: The Rauer group, East Antarctica, *J. Petrol.*, *33*, 693–728.
Harris, A., A. Steffke, S. Calvari, and L. Spampinato (2011), Thirty years of satellite-derived lava discharge rates at Etna: Implications for steady volumetric output, *J. Geophys. Res.*, *116*, B08204, doi:10.1029/2011JB008237.
Harris, N. B. (1982), Skarn Deposits in the Yerington District, Nevada: Metasomatic Skarn Evolution near Ludwig, *Econ. Geol.*, *77*, 877–898.
Harris, N. B., and M. T. Einaudi (1982), Skarn deposits in the Yerington District, Nevada: Metasomatic skarn evolution near Ludwig., *Econ. Geol.*, *77*(4), 877–898.
Heap, M. J., S. Mollo, S. Vinciguerra, Y. Lavallée, K.-U. Hess, D. B. Dingwell, P. Baud, and G. Iezzi (2013), Thermal weakening of the carbonate basement under Mt. Etna volcano (Italy): Implications for volcano instability, *J. Volcanol. Geotherm. Res.*, *250*, 42–60.
Iacono-Marziano, G., F. Gaillard, and M. Pichavant (2007), Limestone assimilation and the origin of CO_2 emissions at the Alban Hills (Central Italy): Constraints from experimental petrology, *J. Volcanol. Geotherm. Res.*, *166*(2), 91–105.
Iacono-Marziano, G., F. Gaillard, and M. Pichavant (2008), Limestone assimilation by basaltic magmas: An experimental re-assessment and application to Italian volcanoes, *Contrib. Mineral. Petrol.*, *155*(6), 719–738.
Iacono-Marziano, G., F. Gaillard, B. Scaillet, M. Pichavant, and G. Chiodini (2009), Role of non-mantle CO_2 in the dynamics of volcano degassing: The Mount Vesuvius example, *Geology*, *37*(4), 319–322.
Iacono-Marziano, G., Y. Morizet, E. Le Trong, and F. Gaillard (2012), New experimental data and semi-empirical parameterization of H_2O–CO_2 solubility in mafic melts, *Geochim. Cosmochim. Acta*, *97*, 1–23, doi:10.1016/j.gca.2012.08.035.
Jamtveit, B. (1991), Oscillatory zonation patterns in hydrothermal grossular-andradite garnet: Nonlinear dynamics in regions of immiscibility, *Am. Mineral.*, *76*(7-8), 1319–1327.

Jamtveit, B., R. A. Wogelius, and D. G. Fraser (1993), Zonation patterns of skarn garnets: Records of hydrothermal system evolution, *Geology*, *21*(2), 113–116.
Jamtveit, B., K. V Ragnarsdottir, and B. J. Wood (1995), On the origin of zoned grossular-andradite garnets in hydrothermal systems, *Eur. J. Mineral.*, *7*, 1399–1410.
Johnston, F. K. B., A. V. Turchyn, and M. Edmonds (2011), Decarbonation efficiency in subduction zones: Implications for warm Cretaceous climates, *Earth Planet. Sci. Lett.*, *303*(1-2), 143–152.
Jolis, E. M., C. Freda, V. R. Troll, F. M. Deegan, L. S. Blythe, C. L. McLeod, and J. P. Davidson (2013), Experimental simulation of magma–carbonate interaction beneath Mt. Vesuvius, Italy, *Contrib. Mineral. Petrol.*, *166*(5), 1335–1353.
Jolis, E. M., V. R. Troll, C. Harris, C. Freda, M. Gaeta, G. Orsi, and C. Siebe (2015), Skarn xenolith record crustal CO_2 liberation during Pompeii and Pollena eruptions, Vesuvius volcanic system, central Italy, *Chem. Geol.*, *415*, 17–36.
Kelemen, P. B., and C. E. Manning (2015), Reevaluating carbon fluxes in subduction zones, what goes down, mostly comes up, *Proc. Natl. Acad. Sci. U. S. A.*, *112*(3), E3997–E4006.
Kelemen, P. B., K. Hanghoj, and A. Green (2014), 4.21 - One view of the geochemistry of subduction-related magmatic arcs, with an emphasis on primitive andesite and lower crust, in *Treatise on Geochemistry*, 2nd ed., edited by H. Holland and K. Turekian, pp. 749–806, Elsevier.
Kerrick, D. M. (1977), The genesis of zoned skarns in the Sierra Nevada, California, *J. Petrol.*, *18*(1), 144–181.
Kerrick, D. M. (2001), Present and past nonanthropogenic CO_2 degassing from the solid Earth, *Rev. Geophys.*, *39*(4), 565–585.
Kerrick, D. M., and K. Caldeira (1998), Metamorphic CO_2 degassing from orogenic belts, *Chem. Geol.*, *145*(3-4), 213–232.
Kuhn, B. (2005), *Scapolite stability: Phase Relations and Chemistry of Impure Metacarbonate Rocks in the Central Alps*, Swiss Fed. Inst. of Technol., Zurich.
Lackey, J. S., J. W. Valley, and J. B. Saleeby (2005), Supracrustal input to magmas in the deep crust of Sierra Nevada batholith: Evidence from high-O zircon, *Earth Planet. Sci. Lett.*, *235*, 315–330.
Lackey, J. S., G. A. Romero, A. S. Bouvier, and J. W. Valley (2012), Dynamic growth of garnet in granitic magmas, *Geology*, *40*(2), 171–174.
Lee, C.-T. A., and J. S. Lackey (2015), Global continental arc flare-ups and their relation to long-term greenhouse conditions, *Elements*, *11*(2), 125–130.
Lee, C.-T. Aet al. (2013), Continental arc-island arc fluctuations, growth of crustal carbonates, and long-term climate change, *Geosphere*, *9*(1), 21–36.
Lee, H., J. D. Muirhead, T. P. Fischer, C. J. Ebinger, S. A. Kattenhorn, Z. D. Sharp, and G. Kianji (2016), Massive and prolonged deep carbon emissions associated with continental rifting, *Nat. Geosci.*, *9*, 1–6, doi:10.1038/NGEO2622.
Liu, Y., Y. Zhang, and H. Behrens (2005), Solubility of H_2O in rhyolitic melts at low pressures and a new empirical model for mixed H2O–CO2 solubility in rhyolitic melts, *J. Volcanol. Geotherm. Res.*, *143*(1-3), 219–235.
Mallik, A., and R. Dasgupta (2014), Effect of variable CO_2 on eclogite-derived andesite and lherzolite reaction at 3 GPa-Implications for mantle source characteristics of alkalic ocean island basalts, *Geochem. Geophys. Geosyst.*, *15*, 1533–1557.
Mallik, A., J. Nelson, and R. Dasgupta (2015), Partial melting of fertile peridotite fluxed by hydrous rhyolitic melt at 2–3 GPa: Implications for mantle wedge hybridization by sediment melt and generation of ultrapotassic magmas in convergent margins, *Contrib. Mineral. Petrol.*, *169*(5), 1–24, doi:10.1007/s00410-015-1139-2.
Marincea, S., D.-G. Dumitras, N. Calin, a. M. Anason, a. M. Fransolet, and F. Hatert (2013), Spurrite, tilleyite and associated minerals in the Exoskarn zone from Cornet Hill (Metaliferi Massif, Apuseni Mountains, Romania), *Can. Mineral.*, *51*(3), 359–375.
Meinert, L. D. (1987), Skarn zonation and fluid evolution in the Groundhog Mine, central Mining District, New Mexico, *Econ. Geol.*, *82*(3), 523–545.
Meinert, L. D. (1992), Skarns and Skarn Deposits, *Geosci. Can.*, *19*(4), 145–162.
Meinert, L. D. (2016), Igneous petrogenesis and skarn deposits, *Geol. Assoc. Can. Spec. Pap.*, *40*, 569–583.
Meinert, L. D., G. M. Dipple, and S. Nicolescu (2005), World skarn deposits, in *Economic Geology. 100th Anniversary Volume*, edited by J. Hedenquist, et al., pp. 299–336. Society of Economic Geologists, Inc., Littleton, Colo.
Menand, T., C. Annen, and M. de Saint Blanquat (2015), Rates of magma transfer in the crust: Insights into magma reservoir recharge and pluton growth, *Geology*, *43*(3), 199–202.
Miyashiro, A. (1974), Volcanic rock series in island arcs and active continental margins, *Am. J. Sci.*, *274*, 321–355.
Moecher, D. P., and E. Essene (1990), Phase equilibria for calcic scapolite, and implications of variable Al-Si disorder for PT, T-X_{CO2}, and a-X relations, *J. Petrol.*, *31*(470), 997–1024.
Moecher, D. P., J. W. Valley, and E. J. Essene (1994), Extraction and carbon isotope analysis of CO_2 from scapolite in deep crustal granulites and xenoliths, *Geochim. Cosmochim. Acta*, *58*(2), 959–967.
Moine, B. N. (1979), La recherche d'anciennes series evaporitiques dans les ensembles metamorphiques, methods et results, *Sci. Terre*, *23*(2), 85–94.
Mollo, S., and A. Vona (2014), The geochemical evolution of clinopyroxene in the Roman Province: A window on decarbonation from wall-rocks to magma, *Lithos*, *192-195*, 1–7, doi:10.1016/j.lithos.2014.01.009.
Mollo, S., M. Gaeta, C. Freda, T. Di Rocco, V. Misiti, and P. Scarlato (2010a), Carbonate assimilation in magmas: A reappraisal based on experimental petrology, *Lithos*, *114*(3-4), 503–514.
Mollo, S., V. Misiti, and P. Scarlato (2010b), Trace element behaviour during interaction between basalt and crustal rocks at 0.5–0.8 GPa: An experimental approach, *Cent. Eur. J. Geosci.*, *2*(2), 188–198.
Mollo, S., M. J. Heap, D. B. Dingwell, K.-U. Hess, G. Iezzi, M. Masotta, P. Scarlato, and S. Vinciguerra (2013), Decarbonation and thermal microcracking under magmatic P-T-f CO2 conditions: The role of skarn substrata in promoting volcanic instability, *Geophys. J. Int.*, *195*, 369–380.
Morgan, B. A. (1975), Mineralogy and origin of skarns in the mount Morrison Pendant, Sierra Nevada, California, *Am. J. Sci.*, *275*, 119–142.
Moussallam, Y., Y. Morizet, M. Massuyeau, M. Laumonier, and F. Gaillard (2014), CO_2 solubility in kimberlite melts, *Chem. Geol.*, *418*, 198–205.
Nadeau, O., A. E. Williams-Jones, and J. Stix (2013a), Magmatic–hydrothermal evolution and devolatilization beneath Merapi volcano, Indonesia, *J. Volcanol. Geotherm. Res.*, *261*, 50–68.
Nadeau, O., A. E. Williams-Jones, and J. Stix (2013b), The behavior of Cu, Zn and Pb during magmatic–hydrothermal activity at Merapi volcano, Indonesia, *J. Volcanol. Geotherm. Res.*, *261*, 50–68.
Newberry, R. J. (1982), Tungsten-bearing skarns of the Sierra Nevada. I. The Pine Creek mine, California., *Econ. Geol.*, *77*(4), 823–844.
Newberry, R. J., M. T. Einaudi, and H. S. Eastman (1991), Zoning and genesis of the Darwin Pb-Zn-Ag skarn deposit, California: A reinterpretation based on new data, *Econ. Geol.*, *86*(5), 960–982.

Ohlhorst, S., H. Behrens, and F. Holtz (2001), Compositional dependence of molar absorptivities of near-infrared OH- and H_2O bands in rhyolitic to basaltic glasses, *Chem. Geol.*, *174*, 5–20.
Pan, Y., M. Fleet, and G. Ray (1994), Scapolite in two Canadian gold deposits; Nickel Plate, British Columbia and Hemlo, Ontario, *Can. Mineral.*, *32*, 825–837.
Papale, P. (1999), Modeling of the solubility of a two-component $H_2O + CO_2$ fluid in silicate liquids, *Am. Mineral.*, *84*, 477–492.
Papale, P., R. Moretti, and D. Barbato (2006), The compositional dependence of the saturation surface of H_2O+CO_2 fluids in silicate melts, *Chem. Geol.*, *229*(1–3), 78–95.
Parks, M. M., S. Caliro, G. Chiodini, D. M. Pyle, T. a. Mather, K. Berlo, M. Edmonds, J. Biggs, P. Nomikou, and C. Raptakis (2013), Distinguishing contributions to diffuse CO_2 emissions in volcanic areas from magmatic degassing and thermal decarbonation using soil gas 222Rn–δ13C systematics: Application to Santorini volcano, Greece, *Earth Planet. Sci. Lett.*, *377-378*, 180–190.
Pascal, M.-L., A. Di Muro, M. Fonteilles, and C. Principe (2009), Zirconolite and calzirtite in banded forsterite-spinel-calcite skarn ejecta from the 1631 eruption of Vesuvius: Inferences for magma-wallrock interactions, *Mineral. Mag.*, *73*(3), 333–356.
Paterson, S. R., D. Okaya, V. Memeti, R. Economos, and R. B. Miller (2011), Magma addition and flux calculations of incrementally constructed magma chambers in continental margin arcs: Combined field, geochronologic, and thermal modeling studies, *Geosphere*, *7*(6), 1439–1468.
Peccerillo, A., M. Federico, M. Barbieri, M. Brilli, and T.-W. Wu (2010), Interaction between ultrapotassic magmas and carbonate rocks: Evidence from geochemical and isotopic (Sr, Nd, O) compositions of granular lithic clasts from the Alban Hills Volcano, Central Italy, *Geochim. Cosmochim. Acta*, *74*(10), 2999–3022.
Pertoldová, J., P. Týcová, K. Verner, M. Košuličová, Z. Pertold, J. Košler, J. Konopásek, and M. Pudilová (2009), Metamorphic history of skarns, origin of their protolith and implications for genetic interpretation: An example from three units of the Bohemian Massif, *J. Geosci.*, *54*(2), 101–134.
Pichavant, M., B. Scaillet, A. Pommier, G. Iacono-Marziano, and R. Cioni (2014), Nature and Evolution of Primitive Vesuvius Magmas: An Experimental Study, *J. Petrol.*, *55*(11), 2281–2310.
Piochi, M., R. A. Ayuso, B. De Vivo, and R. Somma (2006), Crustal contamination and crystal entrapment during polybaric magma evolution at Mt. Somma-Vesuvius volcano, Italy: Geochemical and Sr isotope evidence, *Lithos*, *86*(3-4), 303–329.
Pollington, A. D., and E. F. Baxter (2010), High resolution Sm-Nd garnet geochronology reveals the uneven pace of tectonometamorphic processes, *Earth Planet. Sci. Lett.*, *293*(1-2), 63–71.
Prouteau, G., B. Scaillet, M. Pichavant, and R. Maury (1999), Fluid-present melting of oceanic crust in subduction zones, *Geology*, *27*(12), 1111–1114.
Raimondo, T., C. Clark, M. Hand, J. Cliff, and C. Harris (2012), High-resolution geochemical record of fluid-rock interaction in a mid-crustal shear zone: A comparative study of major element and oxygen isotope transport in garnet, *J. Metamorph. Geol.*, *30*(3), 255–280.
Rasmussen, K. L., D. R. Lentz, H. Falck, and D. R. M. Pattison (2011), Felsic magmatic phases and the role of late-stage aplitic dykes in the formation of the world-class Cantung Tungsten skarn deposit, Northwest Territories, Canada, *Ore Geol. Rev.*, *41*(1), 75–111.
Ray, G. E., and I. C. L. Webster (1997), *Skarns in British Columbia*. Bulletin 101, B.C. Minist. of Employment and Invest., Energy and Miner. Div., Geol. Surv. Branch, Victoria, B. C.
Roberge, J., H. Delgado-Granados, and P. J. Wallace (2009), Mafic magma recharge supplies high CO_2 and SO_2 gas fluxes from Popocatepetl volcano, Mexico, *Geology*, *37*(2), 107–110.
Rosen, O. M., D. Fettes, and J. Desmons (2005), Chemical and mineral compositions of metacarbonate rocks under regional metamorphism conditions and guidelines on rock classification, *Russ. Geol. Geophys.*, *46*(4), 351–360.
Sano, Y., and S. N. Williams (1996), Fluxes of mantle and subducted carbon along convergent plate boundaries, *Geophys. Res. Lett.*, *23*(20), 2749–2752.
Schaaf, P., J. Stimac, C. Siebe, and J. L. Macías (2005), Geochemical evidence for mantle origin and crustal processes in volcanic rocks from Popocatépetl and surrounding monogenetic volcanoes, central Mexico, *J. Petrol.*, *46*(6), 1243–1282.
Shaw, D. M. (1960), The geochemistry of scapolite Part I. Previous work and general mineralogy, *J. Petrol.*, *1*(2), 218–260.
Shishkina, T. A., R. E. Botcharnikov, F. Holtz, R. R. Almeev, A. M. Jazwa, and A. A. Jakubiak (2014), Compositional and pressure effects on the solubility of H_2O and CO_2 in mafic melts, *Chem. Geol.*, *388*, 112–129.
Siswowidjoyo, S., I. Suryo, and I. Yokoyama (1995), Magma eruption rates of Merapi volcano, Central Java, Indonesia during one century (1890–1992), *Bull. Volcanol.*, *57*, 111–116.
Sosa-Ceballos, G., J. E. Gardner, and J. C. Lassiter (2014), Intermittent mixing processes occurring before Plinian eruptions of Popocatepetl volcano, Mexico: Insights from textural-compositional variations in plagioclase and Sr-Nd-Pb isotopes, *Contrib. Mineral. Petrol.*, *167*(2), 1–19, doi:10.1007/s00410-014-0966-x.
Sottili, G., J. Taddeucci, and D. M. Palladino (2010), Constraints on magma–wall rock thermal interaction during explosive eruptions from textural analysis of cored bombs, *J. Volcanol. Geotherm. Res.*, *192*(1-2), 27–34.
Spandler, C., L. Martin, and T. Pettke (2012), Carbonate assimilation during magma evolution at Nisyros (Greece), South Aegean Arc: Evidence from clinopyroxenite xenoliths, *Lithos*, *146-147*, 18–33.
Stolper, E., and J. R. Holloway (1988), Experimental determination of the solubility of carbon dioxide in molten basalt at low pressure, *Earth Planet. Sci. Lett.*, *87*, 397–408.
Thibault, Y., and J. R. Holloway (1994), Solubility of CO2 in a Ca-rich leucitite: Effects of pressure, temperature, and oxygen fugacity, *Contrib. Mineral. Petrol.*, *116*(1-2), 216–224.
Toutain, J.-P., F. Sortino, J.-C. Baubron, P. Richon, Surono, S. Sumarti, and A. Nonell (2009), Structure and CO_2 budget of Merapi volcano during inter-eruptive periods, *Bull. Volcanol.*, *71*(7), 815–826.
Troll, V. R., D. R. Hilton, E. M. Jolis, J. P. Chadwick, L. S. Blythe, F. M. Deegan, L. M. Schwarzkopf, and M. Zimmer (2012), Crustal CO_2 liberation during the 2006 eruption and earthquake events at Merapi volcano, Indonesia, *Geophys. Res. Lett.*, *39*, L11302, doi:10.1029/2012GL051307.
Troll, V. R., et al. (2013), Magmatic differentiation processes at Merapi Volcano: Inclusion petrology and oxygen isotopes, *J. Volcanol. Geotherm. Res.*, *261*, 38–49.
Tsuno, K., and R. Dasgupta (2011), Melting phase relation of nominally anhydrous, carbonated pelitic-eclogite at 2.5–3.0 GPa and deep cycling of sedimentary carbon, *Contrib. Mineral. Petrol.*, *161*(5), 743–763.
Wallace, P. J. (2005), Volatiles in subduction zone magmas: Concentrations and fluxes based on melt inclusion and volcanic gas data, *J. Volcanol. Geotherm. Res.*, *140*(1–3), 217–240.
Wallace, P. J., A. Anderson, T., A. Davis, and M. (1995), Quantification of pre-eruptive exsolved gas contents in silicic magmas, *Nature*, *377*, 612–616.

Watkinson, D. H., and P. Wyllie (1964), The limestone assimilation hypothesis, *Nature*, *204*(4963), 1053–1054.
Watkinson, D. H., and P. J. Wyllie (1969), Phase equilibrium studies bearing on the limestone-assimilation hypothesis, *Geol. Soc. Am. Bull.*, *80*, 1565–1576.
Wenzel, T. (2002), Partial melting and assimilation of dolomitic xenoliths by mafic magma: The Ioko-Dovyren intrusion (North Baikal Region, Russia), *J. Petrol.*, *43*(11), 2049–2074.
White, A. F., T. D. Bullen, D. V. Vivit, M. S. Schulz, and D. W. Clow (1999), The role of disseminated calcite in the chemical weathering of granitoid rocks, *Geochim. Cosmochim. Acta*, *63*(13-14), 1939–1953.
White, A. F., M. S. Schulz, J. B. Lowenstern, D. V. Vivit, and T. D. Bullen (2005), The ubiquitous nature of accessory calcite in granitoid rocks: Implications for weathering, solute evolution, and petrogenesis, *Geochim. Cosmochim. Acta*, *69*(6), 1455–1471.
Yardley, B., and J. Cleverley (2013), *The role of metamorphic fluids in the formation of ore deposits, in Ore Deposits in an Evolving Earth*, edited by G. R. T. Jekin, et al., pp. 117–134, Geol. Soc., London.